Institut für Kernphysik
Goethe-Universität, Frankfurt am Main

MASTER THESIS

Online Drift Velocity Calibration with the Laser System of the ALICE-TPC

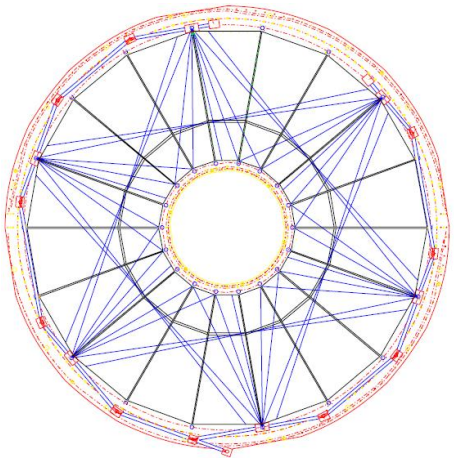

by

Mesut Arslandok

Supervisors:
Prof. Dr. Harald Appelshäuser
Prof. Dr. Hans Rudolf Schmidt

February 11, 2011

ABSTRACT

The ALICE Time Projection Chamber (TPC) is the main tracking detector of ALICE which was designed to perform well at multiplicities of up to 20000 charged primary and secondary tracks emerging from Pb-Pb collisions. Successful operation of such a large and complex detector requires an elaborate calibration and commissioning.

The main goal for the calibration procedures is to provide the information needed for the offline software for the reconstruction of the particle tracks with sufficient precision so that the design performance can be achieved. For a precise reconstruction of particle tracks in the TPC, the calibration of the drift velocity, which in conjunction with the drift time provides the z position of the traversing particles, is essential.

In this thesis, an online method for the calibration of the drift velocity is presented. It uses the TPC Laser System which generates 336 straight tracks within the active volume of the TPC. A subset of these tracks, showing sufficiently small distortions, is used in the analysis. The resulting time dependent drift velocity correction parameters are entered into a database and provide start values for the offline reconstruction chain of ALICE. Even though no particle tracking information is used, the online drift velocity calibration is in agreement with the full offline calibration including tracking on the level of about 2×10^{-4}.

In chapter 2, a short overview of the ALICE detector, as well as the data taking model of the ALICE, is given. In chapter 3, the TPC detector is described in detail. Lastly in chapter 4, the online drift velocity calibration method is presented, together with a detailed description of the TPC laser system.

Contents

1 Introduction

Throughout history, humankind has been trying to answer the questions like; "What is the indivisible component of matter?", "Is the universe infinite or does it have boundaries?", "What is the origin of mass?" and so on. These questions, until the 19th century, were thought to be rather philosophical than scientific. The discovery of the electron, by J.J. Thomson in 1897, ushered in a new age in physics. In the following years one new particle after the other was discovered, mostly as a result of experiments with cosmic rays, the only source of very high energy particles then available.

Today, we are very closer to the answers of these questions than ever before, owing to the development of high energy particle accelerators which enable us to investigate the structure of the matter and produce new particles in the laboratory. There are two reasons for the need to reach high energies. First, a better spatial resolution of the "probe", used to investigate possible structure, requires the beams of high momentum. Second, many of the elementary particles are extremely massive and the energy mc^2 required to create them is correspondingly large [1].

In the early decades of the twentieth century, particle-beam energies from accelerators reached only a few MeV, and their resolution was so poor that protons and neutrons could themselves be regarded as elementary and point like. However, in the early 1970s the deep inelastic electron collision experiments on protons indicated that nucleons (protons and neutrons) have an internal structure—they are built of quarks and gluons [2].

Practically all experimental data from high energy experiments can be accounted for

	Quarks		**Leptons**	
1. Generation	**u** (up)	**d** (down)	e (electron)	ν_e (electron neutrino)
2. Generation	**c** (charmed)	**s** (strange)	μ (muon)	ν_μ (muon neutrino)
3. Generation	**t** (top)	**b** (bottom)	τ (tau)	ν_τ (tau neutrino)

Table 1.1: *Fermions of the Standard Model. Quarks and Leptons come in three generations of doublets.*

by the so called "Standard Model" of particles. According to this model, all matter is built from a small number of fundamental spin 1/2 particles, or fermions: six quarks and six leptons (Table. 1.1). The Standard Model also comprises their interactions (Table. 1.2). The different interactions are described in quantum language in terms of the exchange of characteristic bosons (particles of integer spin) between the fermion constituents. Strong interactions are responsible for binding the quarks in the neutron and proton. Electromagnetic interactions occur between any two particles that have electric charge. Weak interactions are typified by the slow process of nuclear β-decay, involving the emission of an electron and neutrino by a radioactive nucleus [1].

In this sense, the electroweak theory (unified theory of weak and electromagnetic interactions) together with the Quantum Chromodynamics (QCD) form the Standard Model which is a model based on the local gauge group SU(3) $\otimes$ SU(2) $\otimes$ U(1). i.e. the direct product of three simple groups. SU(3) is the gauge group or colour group describing the

Force	Range	Strength	Mediator boson	Mass (GeV)
Electromagnetic	∞	10^{-2}	photon	0
Weak	$< 10^{-18}$ m	10^{-5}	$W^{\pm}$, Z^0	80, 90
Strong	$< 10^{-15}$ m	1	gluon	0

Table 1.2: *A comparison of the range, relative strength, and some properties of mediators of the fundamental forces in the Standard Model.*

strong interactions and SU(2) $\otimes$ U(1) is the gauge group describing the electroweak interactions [3].

The QCD describes the interactions of colored quarks and gluons. The quark model, based on the symmetries and quantum numbers, was introduced by M. Gell-Mann and G. Zweig [4]. It categorizes hadrons (color singlet bound states of quarks, antiquarks and gluons) into two groups; so called "baryons" and "mesons". Mesons are composed of a quark and anti-quark ($q\bar{q}$) while baryons consist of three quarks (qqq) or ($\bar{q}\bar{q}\bar{q}$). The quarks are ruled by the Fermi-Dirac statistics. Since some of the baryons consist of three identical quarks, an additional quantum number was introduced, called color, in order to preserve the Pauli principle. There are three different colors a quark can carry: red, green, and blue. In SU(3) hadronic wave functions are colour neutral states and can be constructed either from color-anti color (mesons) or three different colors (baryons). The strong interaction is mediated between the quarks by eight massless gauge bosons called gluons. The fundamental difference from the electromagnetic interaction, where the photon itself carries no electrical charge, is that gluons themselves carry color charges. It follows that gluons do not interact only with quarks but also couple to the color charges of other gluons, which is the reason for many special properties of the strong interaction.

The demand for color neutrality also means that individual quarks can not be observed. To separate a single, color-charged quark from a hadron would require an infinite work done against the color field. This increases the energy of the color field to such an extent that new quark-antiquark pairs i.e. mesons are created out of the vacuum to keep the color-neutral form of the hadron. This phenomenon is called ***color confinement*** or ***confinement***.

The strength of the strong interaction is given by the QCD running coupling constant:

$$\alpha_s(q^2) = \frac{12\pi}{(33 - 2n_f) \cdot ln\left(q^2/\Lambda^2_{QCD}\right)} \tag{1.1}$$

where q is the momentum transfer in deep inelastic scattering, n_f is the number of the participating quark flavors and Λ_{QCD} ($\sim$ 250 MeV/c) is a free parameter, which must be determined experimentally [5]. In case of large momentum transfer ($q^2 \to \infty$) i.e. asymptotically short distances, the coupling vanishes. In these circumstances quarks can be regarded as free particles. This is known as ***asymptotic freedom*** [6], which explains scaling at short distances and offers a mechanism for confinement at large distances (Wilczeck and Politzer, Nobel Price in 2004).

The Lattice QCD, which is a method for calculating equilibrium properties of strongly interacting systems directly from the QCD Lagrangian by numerical evaluation of the corresponding path integrals, predicts that, at sufficiently high energy densities, there will be a transition from hadronic matter to a plasma of deconfined quarks and gluons. This is the so called Quark Gluon Plasma (QGP). Within the framework of the Standard Model,

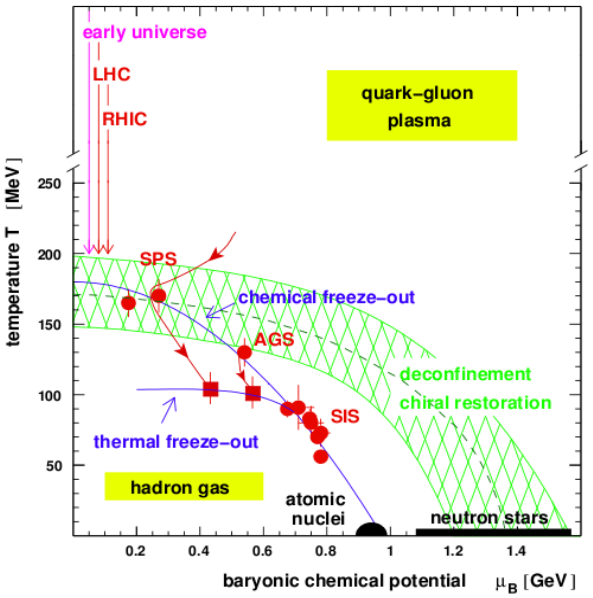

Figure 1.1: *The phase diagram of QCD [7].*

the appearance of phase transitions involving elementary quantum fields is intrinsically connected to the breaking of fundamental symmetries of nature and thus to the origin of mass.

Fig. 1.1 shows the phase diagram of strongly interacting matter in the temperature vs. baryon chemical potential plane (T, μ_B). At high temperature T and vanishing μ_B, qualitative aspects of the transition to the QGP are controlled by the chiral symmetry of the QCD Lagrangian. In the limit of vanishing quark masses the QCD Lagrangian is chirally symmetric, i.e. invariant under separate flavor rotations of right and left-handed quarks. Lattice calculations suggest that this crossover is rather rapid, taking place in a narrow temperature interval around $T_c \sim 170$ MeV. At T_c two phenomena happen simultaneously; color confinement is broken, i.e. colored degrees of freedom can propagate over distances much larger than the size of a hadron, and the approximate chiral symmetry of QCD, which is spontaneously broken at low temperatures and densities, gets restored [7]. On the other hand, at low temperatures and asymptotically large baryon densities quarks are also deconfined, although not in a quark-gluon plasma state but rather in a color superconductor [8].

In ultra-relativistic heavy-ion collisions, one expects to attain energy densities which reach and exceed the critical energy density ε_c (~ 1 GeV), thus making it possible to study the QCD phase transition and the physics of the Quark-Gluon Plasma (QGP) state. The system created in heavy-ion collisions undergoes a fast dynamical evolution from the extreme initial conditions to the dilute final hadronic state. The space-time evolution of an ultrarelativistic heavy ion collision is shown in Fig.1.2.

At the first instants of the collision, called pre-equilibrium, the energy deposited in the collision volume is redistributed into other degrees of freedom. After the so called "formation time" (~ 1 fm/c), the deposited energy may lead to the formation of the QGP. As the reaction zone expands, the collision fireball cools down and goes through a mixed phase in which the formed hadrons coexist with the deconfined quarks and gluons. Finally, all quarks and gluons condensate into a state of the highly interacting hadron gas which

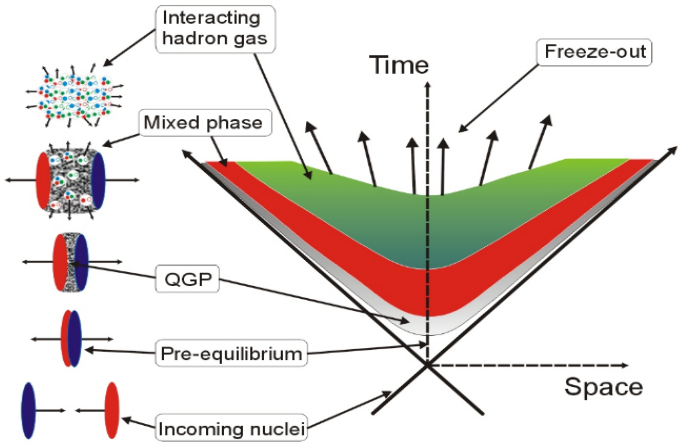

Figure 1.2: *Space-time diagram for nucleus-nucleus collision, showing the various stages of the evolution of expanding matter [9].*

further expands and cools to the point called chemical freeze-out, where the last inelastic collisions occur. At this point abundances of all hadrons are fixed and only elastic collisions between particles continue. The final stage where all elastic collisions vanish (thermal freeze-out) is reflected in the momenta of the measured particles [9].

Since heavy ion collisions are highly complex processes, connections with other fields of physics may also show up and become important [2]. Maybe, the most striking connection is to the studies on the models of the early universe. According to Big-Bang cosmology, the universe evolved from an initial state of extreme energy density to its present state through rapid expansion and cooling, just as in the case of ultra relativistic heavy ion collisions. It is believed that the QGP phase existed in the early universe up to few microseconds after the Big Bang. Moreover, the knowledge of the equation of state for nuclear matter at extreme density is relevant for astrophysics, in understanding the dynamics of supernovae explosions and the stability of neutron stars [10]. In this sense, the information that can be extracted from ultra relativistic heavy ion reactions may provide a deeper insight into the models of the early universe and astrophysical phenomena.

The Large Hadron Collider (LHC) provides an ideal tool for the study of this "new state of matter, QGP". It brings heavy-ion physics into such a high energy region ($\sqrt{s} = 5.5$ TeV per nucleon pair in Pb-Pb collisions) that the net baryon density in the central rapidity region vanishes and the experimental conditions become close to the ones of lattice QCD calculations as well as to those of the expanding early universe.

Even though the standard model accounts for an enormous body of experimental data, as a complete theory of physics it does have some significant shortcomings. For instance, it does not include gravity and has nearly twenty parameters that cannot be calculated within its framework. Also, in the standard model, neutrinos are assumed to be massless, but there is growing evidence, from the solar and atmospheric anomalies, that neutrinos do have finite masses [1]. In other words, it appears that in trying to understand some of the major features of our universe, such as the preponderance of 'dark matter' and the large matter-antimatter asymmetry, we will also require new and presently unknown physics beyond that of the Standard Model. That is to say, relativistic heavy ion collisions will quite likely come along with some suprising results.

2 A Large Ion Collider Experiment (ALICE)

2.1 Role of ALICE in the LHC Experimental Programme

The Large Hadron Collider (LHC), designed to collide protons at a c.m.s. energy $\sqrt{s} =$ 14 TeV, will also accelerate ions up to the same magnetic rigidity and allow the study of both symmetric systems (e.g. Pb-Pb) and asymmetric collisions, such as proton-nucleus. One of the central problems addressed at the LHC is the connection between phase transitions involving elementary quantum fields, fundamental symmetries of nature and the origin of mass. The experimental programme at the LHC addresses both aspects of the symmetry-breaking mechanism through complementary experimental approaches.

ALICE [11] will study the role of chiral symmetry breaking in the generation of mass in composite particles (hadrons) using heavy-ion collisions. It has been specifically designed to study the physics of strongly interacting matter and particularly the QCD phase diagram and the properties of the QGP phase in an interaction environment with large charged-particle multiplicities. The experiment has been designed to cope with up to 8000 charged particles per unit rapidity at mid-rapidity in Pb-Pb collisions at $\sqrt{s} = 5.5$ TeV per nucleon pair [12, 10, 13].

On the other hand, the successful completion of the heavy-ion programme requires the study of p-p, p-A and lighter A-A collisions in order to establish the benchmark processes under the same experimental conditions. Besides, these measurements are interesting in themselves. For example, the study of lighter systems opens up possibilities to study fundamental aspects of the interaction of colour-neutral objects related to non-perturbative strong phenomena, like confinement and hadronic structure. Also, due to its excellent tracking and particle identification capabilities, the ALICE p-p and p-A programs complement those of the dedicated p-p experiments.

2.2 General Overview of ALICE and its Subdetectors

ALICE is a general-purpose heavy-ion experiment at the LHC. Its detectors measure and identify mid-rapidity hadrons, leptons and photons produced in an interaction environment with large charged-particle multiplicities [14].

The detector acceptance is sufficiently large to enable the study on an event-by-event basis of particle ratios, p_t spectra and HBT (Hanbury–Brown–Twiss) correlations. This implies tracking of several thousand particles in every event. ALICE is capable of tracking and identifying particles from very low (~ 100 MeVc^{-1}) up to fairly high (~ 100 GeVc^{-1}) transverse momentum (p_t). The detectors use mostly three-dimensional hit information and continuous tracking with many points in a nominal magnetic field $|B| \leq 0.5$ T.

The ALICE detector consists of the the following subdetectors and magnets (Fig. 2.1):

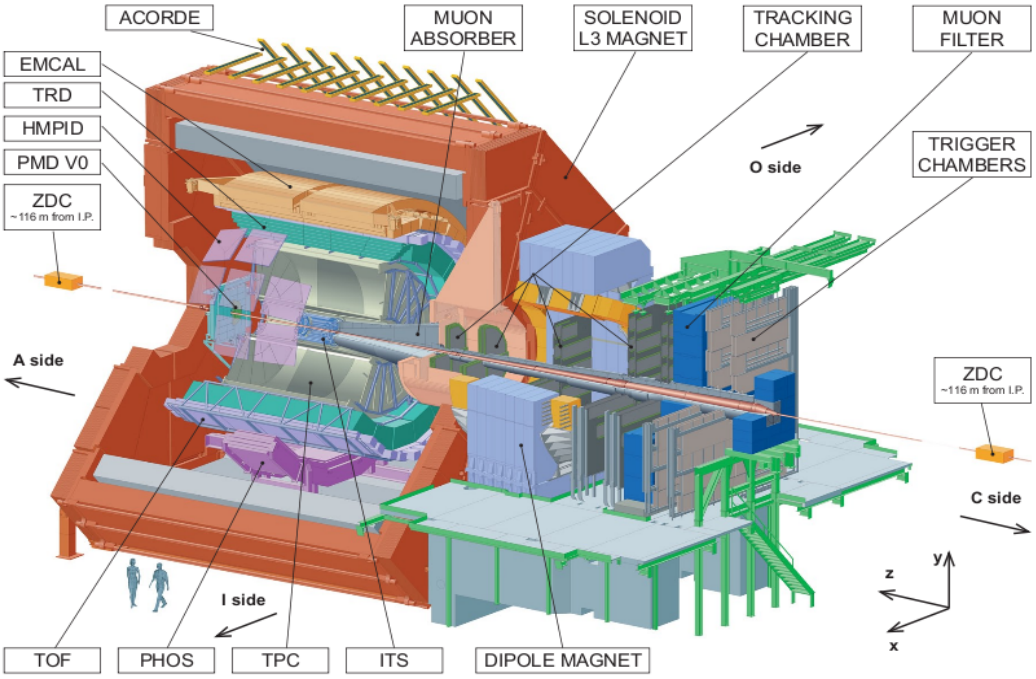

Figure 2.1: *ALICE schematic layout [15].*

2.2.1 Magnets

The ALICE experiment uses two large magnets:

- The central part of the detector is enclosed in a solenoid magnet with the nominal field of 0.5 T along the beam direction, with almost-zero radial components.
- A large dipole magnet with resistive coils and a horizontal field perpendicular to the beam axis is used for the muon spectrometer. The field integral in the forward direction is 3 Tm.

2.2.2 Central Detectors

Inner Tracking System (ITS)

The ITS is composed of six cylindrical layers of silicon detectors, located at radii between 4cm and 44cm [16]. The main purpose of these layers starting from the beam pipe are:

Silicon pixel layers (SPD): The silicon pixel detector SPD constitutes the two innermost layers of the ITS. They are fundamental elements for the determination of the primary vertex as well as for measurement of the impact parameter of secondary tracks originating from weak decays of strange, charm and beauty particles.

Silicon drift layers.(SDD): The silicon drift detector SDD equips the two intermediate layers of the ITS. They have a very good multitrack capability and provide two out of the four dE/dx samples needed for the ITS particle identification.

Silicon Strip Detectors (SSD): The SSD represents the two outermost layers equipped with double-sided silicon microstrip detectors. The SSD is crucial for the matching of tracks from the TPC to the ITS. It also provides dE/dx information to assist particle identification for low-momentum particles.

Time-Projection Chamber (TPC)
The TPC is the main tracking detector of the ALICE central barrel [17]. The main goal of the TPC is to provide charged-particle momentum measurements with good two-track separation, particle identification, and vertex determination together with the other central barrel detectors. A detailed description of TPC will be given in chapter 3.

Transition Radiation Detector (TRD)
The main goal of the TRD [18] is to provide electron identification in the central barrel for momenta above 1 GeVc^{-1} where the pion rejection capability through energy loss measurement in the TPC is no longer sufficient. Further, it is used as a fast trigger for charged particles with high momentum.

Time-Of-Flight (TOF) detector
The TOF detector [19], which is a large area array of Multi-gap Resistive-Plate Chambers (MRPC) surrounding the TRD, improves the Particle Identification (PID) in the intermediate momentum range from 0.2 to 2.5 GeVc^{-1}. Coupled with the ITS and TPC for track and vertex reconstruction and for dE/dx measurements in the low-momentum range (up to about 0.5 GeVc^{-1}), it provides event-by-event identification of large samples of pions, kaons, and protons.

High-Momentum Particle Identification Detector (HMPID)
The goal of the HMPID, a Ring Imaging Cherenkov detector (RICH), is to enhance the PID capability of ALICE beyond the momentum range attainable through the energy loss (in ITS and TPC) and time of flight (in TOF) measurements [20].

PHOton Spectrometer (PHOS)
The PHOS [21] is a high-resolution electromagnetic spectrometer. It detects electromagnetic particles in a limited acceptance domain at central rapidity and provide photon identification as well as neutral mesons identification.

ElectroMagnetic CALorimeter (EMCal)
The EMCal [22] is a large Pb-scintillator sampling calorimeter with cylindrical geometry. It improves the jet energy resolution and increases the existing ALICE capabilities to measure high-momentum photons and electrons.

ALICE COsmic Ray DEtector (ACORDE)
ACORDE is an array of plastic scintillator counters placed on the upper surface of the L3 magnet. It detects, in combination with the TPC, TRD and TOF, single atmospheric muons and multi-muon events, so-called muon bundles. Further, it provides a fast L0 trigger signal, when atmospheric muons impinge upon the ALICE detector [11].

2.2.3 Forward Detectors

Muon Spectrometer
The muon spectrometer [23] is dedicated to the analysis of heavy quark resonances (J/Ψ and Ψ', Υ, Υ' and Υ'') in the $\mu^+\mu^-$ decay channel. It consists of a passive front absorber to absorb hadrons and photons from the interaction vertex, a high-granularity tracking

system of 10 detection planes, a large dipole magnet, a passive muon filter wall, followed by four planes of trigger chambers and an inner beam shield to protect the chambers from particles and secondaries produced at large rapidities [11].

Zero Degree Calorimeter (ZDC)
The number of participant nucleons is the observable most directly related to the geometry of the collision [24]. This quantity can be estimated by measuring the energy carried in the forward direction by non-interacting (spectator) nucleons. The ZDC detects these spectator nucleons and thus provides information about the event centrality. It is also used as a fast trigger to enhance the sample of central collisions.

Photon Multiplicity Detector (PMD)
The PMD consists of a preshower detector with a charged particle veto detector in front [25]. It measures the multiplicity and spatial $(\eta - \phi)$ distribution of photons on an event-by-event basis. It addresses physics issues related to event-by-event fluctuations, flow and formation of Disoriented Chiral Condensates (DCC) and provides estimates of the transverse electromagnetic energy and the reaction plane.

Forward Multiplicity Detector (FMD)
The silicon strip Forward Multiplicity Detector (FMD) provides (offline) charged-particle multiplicity information [26]. High radial detector segmentation allows for the study of multiplicity fluctuations on an event-by-event basis while azimuthal segmentation allows for the determination of the reaction plane for each event and the analysis of flow within the FMD's pseudo-rapidity coverage. Further, it can be used as a trigger at the L2 trigger level or above (due to a readout time of ~ 13 μs).

V0 detector
The Vertex0 detector V0 is a small angle detector consisting of two arrays of scintillator counters, called V0A and V0C, that are installed on either side of the ALICE interaction point [26]. It provides a minimum bias trigger for the central barrel detectors in p-p and A-A collisions and two centrality triggers in Pb-Pb collisions at the level L0. It serves as a centrality indicator via the multiplicity recorded in the event. Further, it provides background rejection for the di-muon spectrometer and contributes to the rejection of beam-gas interactions..

T0 detector
The Time0 detector (T0) consist of Cherenkov counters [26]. It generates a T0 signal for the TOF detector with a required precision about 50 ps. It measures the vertex position (with a precision ± 1.5 cm) for each interaction and provides a L0 trigger when the position is within the preset values. It gives a fast evaluation of the multiplicity in A-A collisions. Furthermore, It provides an early 'wake-up' signal to TRD, prior to L0.

2.3 ALICE Coordinate Systems

Global Coordinates: The ALICE coordinate system is a right-handed orthogonal cartesian system whose origin is taken to be the beam interaction point (IP). Its x coordinate is perpendicular to the mean beam direction such that the positive x is pointing to the center of the accelerator, y coordinate is perpendicular to the mean beam direction point-

ing upward and z coordinate is parallel to the mean beam direction such that positive z pointing towards the Shaft side (RB24) and negative z towards the Muon Arm (RB26).

The Azimuthal angle φ increases counterclockwise, starting from the x-axis ($\varphi = 0$) to

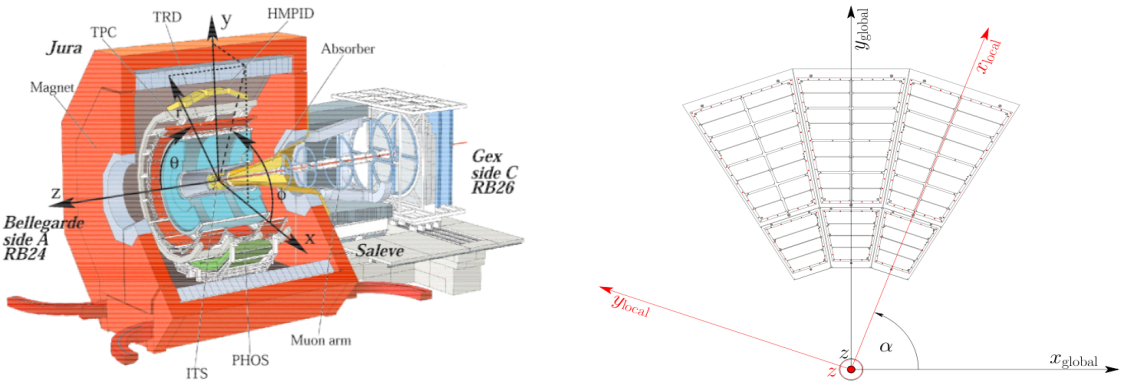

Figure 2.2: *Sketch of the ALICE global (left) and local (right) coordinate systems [27, 28].*

y-axis ($\varphi = \pi/2$) for an observer standing at positive z and looking to the Muon Side. The polar angle θ increases from the z-axis to the xy plane [27, 29].

The following are the definition of some sides of the ALICE experiment:
A side : positive z (shaft side),
C side : negative z (muon side),
I side : positive x (towards LHC center, Inner),
O side : negative x (towards Jura, Outer).
U side : positive y (Up)
D side : negative y (Down)

Local Coordinates: The local offline coordinate system is used to account for the azimuthal segmentation of the central barrel detectors. It is a right handed cartesian system which has the same origin and the same z-axis as the global system. The local system is rotated such that the x-axis is perpendicular to the sub-detectors 'sensitive plane' (TPC pad row, ITS ladder etc.). Therefore the local and global systems can be transformed into each other by a simple rotation of the angle α around the z-axis. In case of the TPC, the x-axis points radially outwards and the y-axis completes the right-handed cartesian system by being parallel to the pad rows. The transformation is done with $\alpha = sector \times 20°$:

$$x_g = x_l.\cos(\alpha) - y_l.\sin(\alpha) \quad (2.1)$$
$$y_g = y_l.\cos(\alpha) + x_l.\sin(\alpha) \quad (2.2)$$

A sketch of the local and global coordinate systems are shown in Fig. 2.2.

2.4 Data Taking Model

During the data taking process [14], the whole experiment is steered by the Experiment Control System (ECS). The ECS is responsible for the synchronization between the four ALICE online systems; Data Acquisition system (DAQ), Trigger system (TRG), High Level Trigger system (HLT) and Detector Control System (DCS). This is schematically shown in

Fig. 2.3. The running conditions, partitioning, run type, run number and trigger settings are propagated from ECS to DCS before the start of each run. The partitioning allows different groups of subdetectors to be read out with different triggers concurrently such that one subdetector can only join one partition but more than one trigger cluster at a time.

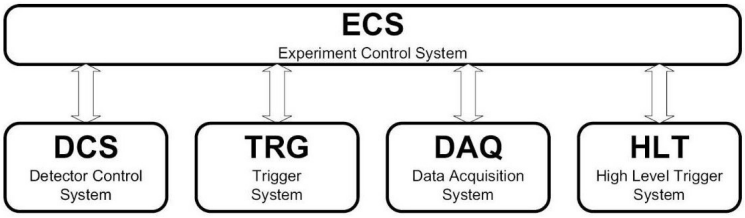

Figure 2.3: *Schematic overview of the ALICE online systems [15].*

A run type defines how the FEE will be configured and which subsystems are to be activated at the start of the run. A "Physics Run" is the general run type for recording data with beam-beam collisions. The remaining run types are used for the calibration purposes (e.g. in case of TPC pedestal, pulser and laser calibration runs).

DCS: The DCS provides remote control and monitoring of all detector equipment in such a way that the whole the ALICE detector (also each sub-detector) can be operated from a single workplace, the ALICE Control Room (ACR) at LHC Point 2. The primary tasks of the DCS are to ensure safe and reliable operation of ALICE and to provide optimal operational conditions to attain high quality data. For this, the required information is retrieved from the DCS databases.

Trigger System: Since ALICE studies several physics topics using different beam conditions, a large number of trigger classes are used to select and characterize the events with respect to the requirements and the restrictions imposed by the bandwidth of the DAQ and the HLT. Trigger inputs are pulses provided by the trigger detectors so as to be synchronized to the LHC clock cycle, as distributed by the Timing, Trigger and Control (TTC) system. The trigger decision, made within in 100 ns, is provided by the Central Trigger Processor (CTP). The CTP handles this process concurrently for the different trigger clusters.

The ALICE trigger system is based on three trigger levels; Level-0 (L0), Level-1 (L1) and Level-2 (L2) with the response of "accept" or "reject";

- **L0:** It has a fixed latency of about 1.2 μs with respect to the interaction.
- **L1a/L1r:** Each L0 can be followed by a L1 pulse after a fixed latency of about 7.7 μs with respect to the interaction time. In case of L1r the trigger sequence is terminated. If an L1a was issued, an asynchronous message containing basic event information (containing the event ID) will follow.
- **L2a/L2r:** L2 completes the trigger sequence by deciding if the triggered event should be transferred from the FEE data buffers to the DAQ. This trigger level is dispatched as an asynchronous message after a minimum time of about 92 μs, which corresponds to the TPC drift time, in order to ensure the completion of the TPC readout. Further,

L2 trigger waits for the end of the past-future protection interval (e.g. ± 10 μs for the ITS and 92 μs for the TPC in case of p-p) to verify that the event can be taken. The purpose of the past-future protection circuit is to ensure that the events selected for readout are not spoiled by pile-up.

The Data Acquisition: The detectors receive the trigger signals and the associated information from the Central Trigger Processor (CTP), through a dedicated Local Trigger Unit (LTU) interfaced to the TTC system. The readout electronics of the all detectors is interfaced to the ALICE-standard Detector Data Links (DDL). At the receiving side of the DDLs there are so called 'DAQ Readout Receiver Card' (D-RORC) hosted by the front-end machines, called Local Data Concentrators (LDCs). The event fragments originated by the various D-RORCs are logically assembled into sub-events in the LDCs which is also capable of local data recording, if used in stand-alone mode, and online sub-event monitoring. The LDCs ship the sub-events to a farm of machines called Global Data Collectors (GDCs) where the whole events are built from all the sub-events pertaining to the same trigger. GDCs then send these events to the Permanent Data Storage (PDS). In addition, the GDC is capable of online event monitoring.

The Data Acquisition and Test Environment (DATE) is the DAQ software framework which controls and synchronizes the processes running in the LDCs and the GDCs. It can run on an LDC, a GDC or another computer.

HLT: Since the event rate is limited by the Data Acquisition (DAQ), an on-line processing is necessary, in order to reduce the data size. For this purpose the HLT system was designed. The HLT allows forwarding zero-suppressed events into the DAQ data stream on an event-by-event and detector-by-detector basis. All subdetectors submit their data into the HLT upon a L2 accept. The HLT system receives a copy of all the raw data from the LDCs. Firstly, It accepts or rejects events based on detailed online analysis by providing a trigger decision. Secondly, it selects relevant parts of the (sub-) event or regions of interest. Then it reduces the event size by applying compression techniques on the accepted and selected data. Lastly, the output is submitted to the event builders for permanent storage. A key requirement of the system is the ability to process the event analysis in real-time [30].

Reconstruction: The offline framework handles the offline analysis and the reconstruction of the physics data coming from simulated and real interactions. This is carried out by the ALICE computer framework "AliRoot", which makes use of the object oriented, C++ based ROOT framework [31].

The detected hits, energy depositions at a given point and time, are stored for each detector and they are later on converted into digits taking into account the detector and associated electronics response function. As an input, the reconstruction uses the digits that are the digitized signals (ADC counts) obtained by a sensitive pad of a detector at a certain time, together with some additional information like module number, readout channel number, time bucket number, etc. The digits could be in both ROOT format, which is more convenient for development and debugging purposes, and raw data format, as they are output from the detector or can be generated from simulated special-format digits (see Fig. 2.4).

First, a local reconstruction of clusters, containing the space point information of the particles, is performed in each detector. Then vertices and tracks are reconstructed and the particle identification is carried on. The combined track finding, which is based on the Kalman Filter approach (a method for simultaneous track recognition and reconstruction),

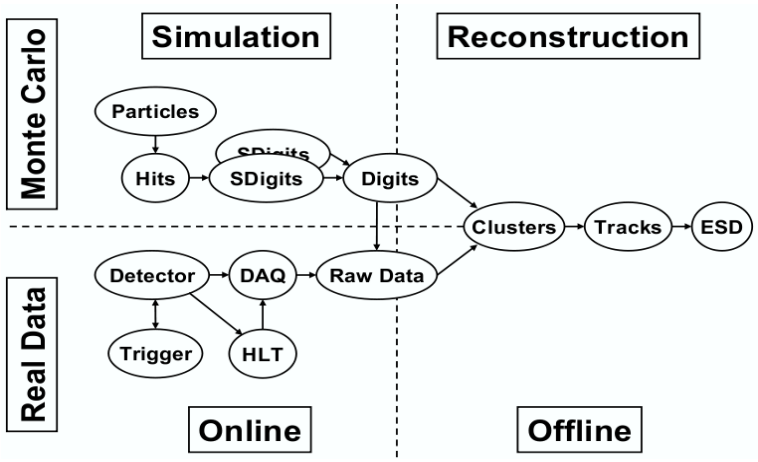

Figure 2.4: *Reconstruction process up to ESDs [31].*

in the central ALICE detectors consists of three steps (Fig. 2.5):

1. *Initial inward reconstruction pass:* Track seeding in the outermost pad rows of the TPC to the primary vertex through the ITS layers.
2. *Outward reconstruction pass and matching with the outer detectors:* Tracking from the innermost ITS layer to the outer detectors; TOF, HMPID, PHOS and EMCAL.
3. *Final reconstruction pass:* Refitting the primary tracks back to the primary vertex or, in the case of the secondary tracks, as close to the vertex as possible.

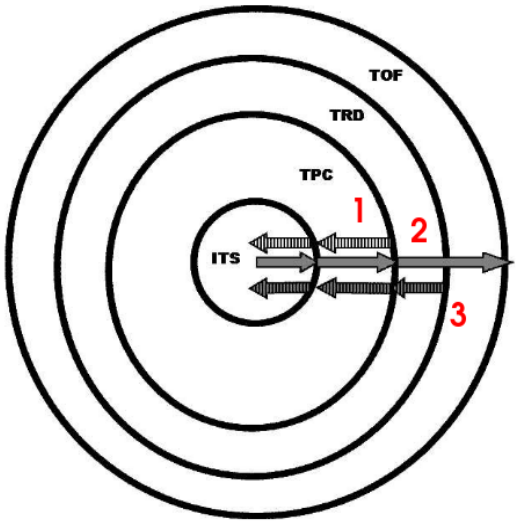

Figure 2.5: *Schematic view of the three passes of the combined track finding [31].*

Finally, the outcome of the reconstruction process is kept in a structure, so called Event Summary Data (ESD), containing the reconstructed charged particle tracks (together with the particle identification information), decays with the V^0, kink and cascade topologies and some neutral particles reconstructed in the calorimeters, as well as the global event properties [32].

3 The Time Projection Chamber (TPC)

3.1 Layout of the TPC

The ALICE Time Projection Chamber [17], the largest TPC built so far with the volume of 88 m^3, is the main tracking, pattern recognition, and particle identification device in ALICE. It was designed to perform well at multiplicities of up to $dN_{ch}/d\eta = 8000$, which would result in 20000 charged primary and secondary tracks emerging from Pb-Pb collisions at a center of mass energy of $\sqrt{s} = 5.5$ TeV. The TPC covers the momentum range $0.1 - 100$ GeVc^{-1} within the pseudo rapidity range $|\eta| < 0.9$.

The main performance goals of the TPC are; track matching efficiency with inner and outer detectors at the level of 85-95%, the dE/dx resolution lower than 10%, the relative p_t resolution of about 1% at 2 GeV/c and a two track-resolution capable of separating tracks with a relative momentum below 5 MeV. Further, the readout rate for p-p collisions is expected ~ 1 kHz, while for Pb-Pb collisions ~ 0.2 kHz.

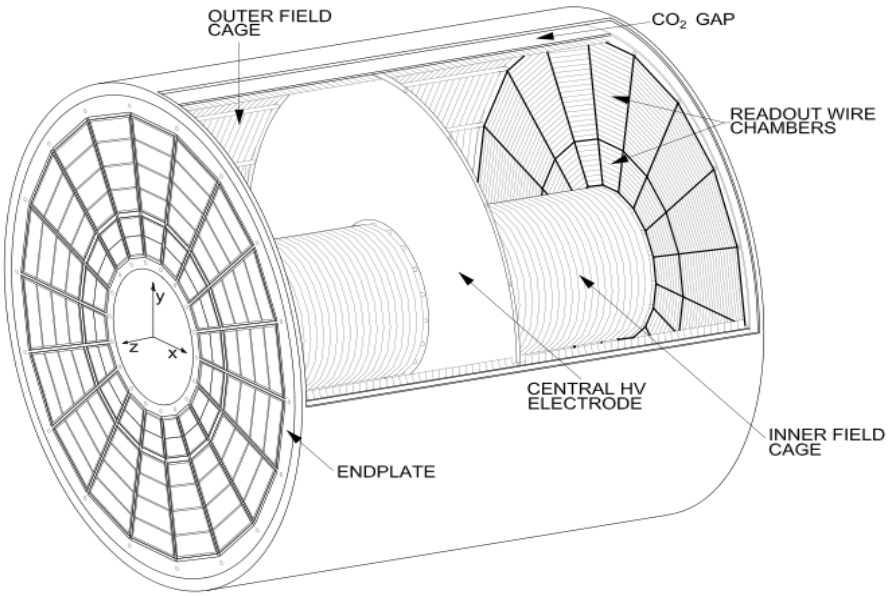

Figure 3.1: *Layout of the TPC field cage [15].*

The layout of the TPC is shown in Fig. 3.1. The TPC, which has an active radial range from about 85 to 250 cm, and an overall length along the beam direction of 500 cm, is made of a large cylindrical vessel filled with a gas mixture of Ne-CO_2-N_2. It is divided equally into two readout sides (A- and C- Side) by a 100 kV central electrode (CE). The readout chambers are positioned on the endplates.

3.1.1 Field Cage

The main purposes of the field cage [15, 33, 34] are to define a uniform electrostatic field in the gas volume and together with the Service support Wheel (SSW) to provide a stable mechanical structure for precise positioning of the chambers and other detector elements.

The TPC field cage is housed in two outer cylinders (outer containment vessel, outer field cage vessel) and two inner cylinders (inner field cage vessel, inner containment vessel). It is comprised of the central electrode (CE), the field strips which are connected by a voltage divider network and 72 rods, whose main role is to hold the field cage strips, positioned axially on the internal walls of the inner and outer field-cage vessels. The electrical isolation of the field cage is provided by CO_2 filled gas gaps between the containment vessels and the field cage vessels. At the center of the field cage the central electrode, made of a stretched 30 μm thick aluminised mylar foil, is located perpendicularly to the beam axis with a mechanical stability and precision of 250 μm in the position (Fig. 3.1).

Owing to the choice of the gas composition used in the TPC, the field cage has to be operated at a rather high drift field 400 V/cm, with a high voltage of 100 kV at the CE. This results in a drift time of about 92 μs. Two opposite axial potential degraders with potential strips provides the uniformity of the drift field on either side of the central electrode. This minimizes the electric field distortions inside the drift volume. The field shape distortions inside the drift volume are below 10^{-4} at a distance of 15 mm from the strips.

3.1.2 Readout Chambers

The overall design of the readout plane, which is based on conventional multi-wire proportional counters, has been optimized with respect to the high multiplicity environment of a central Pb-Pb collisions. The azimuthal segmentation of the readout plane is common with the subsequent ALICE detectors TRD and TOF, i.e. 18 trapezoidal sectors, each covering 20° in azimuth. Further, the radial dependence of the track density leads to a radial segmentation of the readout plane into Inner (IROC) and Outer (OROC) ReadOut Chambers within one sector. The TPC thus has 36 sectors each having 159 radial pad rows, resulting in a total of 570132 pads and a total active area of ~ 32.5 m^2.

Chamber Type	Pad Size [mm^2]	Number of Pad Rows
IROC (81.1 – 132.1 cm)	4×7.5	63
OROC (134.6 – 198.6 cm)	6×10	64
OROC (198.6 – 246.6 cm)	6×15	32

Table 3.1: *Pad sizes and number of pad rows within a sector.*

In the offline code a specific numbering convention [29], (If not explicitly stated) with the view point of the interaction point, is used for 72 ROCs as seen in Fig. 3.3. Numbering always starts with zero, from left to right, and from bottom to top. For instance, the pads are aligned in rows numbering from left to right while the padrows from bottom to top.

The readout chambers [15] are made of standard wire planes; a grid of anode wires above the pad plane, a cathode-wire grid, and a gating grid facing the drift volume. All wires run in the azimuthal direction. Since the design constraints are different for the inner and outer chambers, their wire geometry is different (Fig. 3.2).

In view of cost and the granularity resulting from the diffusion, the pad size cannot be

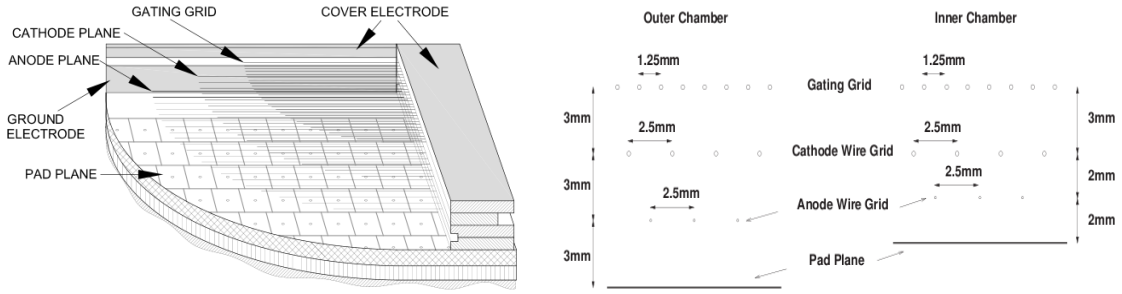

Figure 3.2: *Cross section through a readout chamber showing the pad plane, the wire planes and the cover electrode (left). Wire geometries of the outer and inner readout chambers (right) [15].*

chosen arbitrarily. The goal is to find a pad configuration for which the resulting single-track cluster area is minimal. The readout pad structure, therefore, has been optimized for signal-to-noise ratio and position resolution at the desired gas gain. The adopted pad sizes and number of pad rows, as well as the effective active radial length (taking edge effects into account) of the ROCs are summarised in Table 3.1.

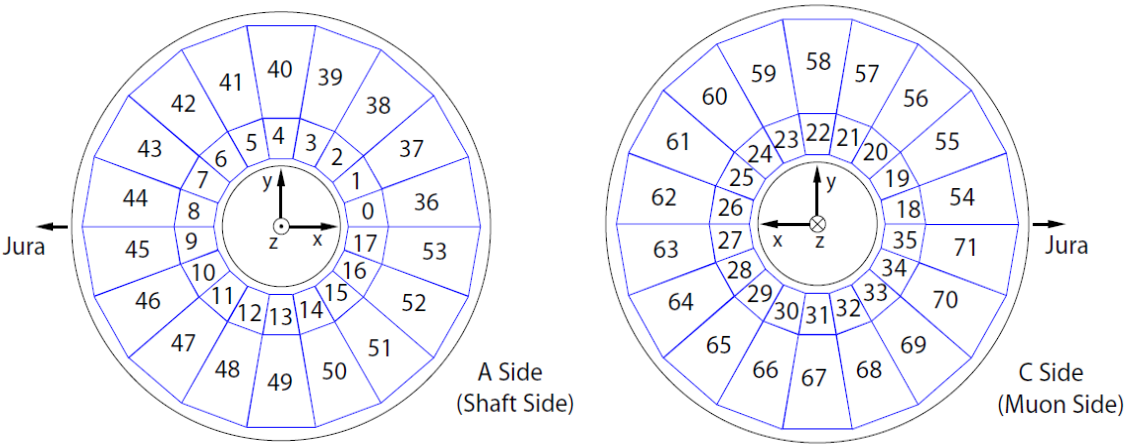

Figure 3.3: *Numbering of the 72 ROCs in the offline code [29].*

3.1.3 Front End Electronics (FEE)

The front-end electronics (FEE) reads out the charge detected by the 570132 pads from the cathode pad plane of the readout chambers. The FEE can be divided into two parts; the front end cards (FECs) and the readout control units (RCUs).

FEC: The actual signal processing is done by the FECs located 7 cm away from the pad plane via flexible Kapton cables. The FEC contains the complete readout chain for the amplification, shaping, digitization, processing and buffering of the TPC signals. The main parts of the FEC are Pre-Amplifier and Shaper chips (PASAs) and Alice TPC Readout Chips (ALTROs) each of which handles 16 channels. Each FEC houses 8 PASAs and 8 ALTRO chips, 128 channels in total [35].

A scheme of the data flow of one channel is displayed in Fig. 3.4. The charge signal from the pads is passed to the FECs and transformed into a differential semi-Gaussian

voltage signal by the PASA with a rise time of 120 ns and a shaping time (FWHM) of about 190 ns. Each channel of the ALTRO chip has three components; a 10 bit Analogue-Digital- Converter(ADC), a digital circuit with several digital filters and a multi event buffer. The output signal of the PASA chip is digitized by a 10 bit ADC capable of 10 million samples per second. The digitized signal is then processed by a set of circuits that perform: first baseline correction, tail cancellation, second baseline correction, zero suppression and data formating, respectively. An important feature is that processing parameters and algorithms can be reconfigured.

RCU: One TPC sector is subdivided into 6 partitions; two for the IROC and four for the OROC each controlled by one RCU. Depending on the radial position in the sector, one partition may have 18 to 25 FECs. The RCU provides core functionality to configure, trigger, readout, monitor and debug the FEE. It acts as a bridge between the FECs and the DAQ, DCS and the trigger system of the TPC. Data are forwarded from the RCU by means of an optical fiber, the Detector Data Links (DDL), to the DAQ. A DCS board equipped with an embedded ARM processor running Linux is attached to the RCU for control and monitoring. From the readout and control point of view, each partition represents an independent system.

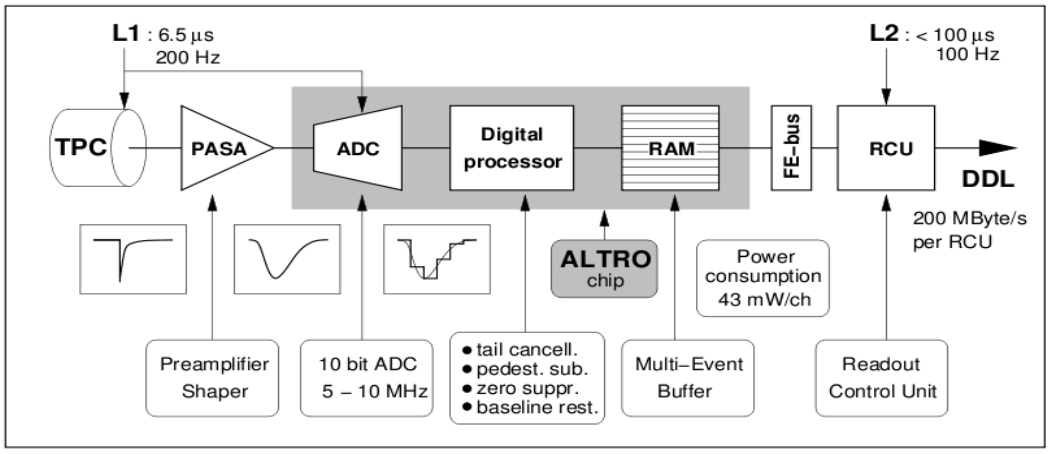

Figure 3.4: *Block diagram of the TPC front-end electronics [14].*

The TPC data acquisition is started either upon a Level-0 or upon a Level-1 trigger, according to the configuration of the trigger detectors participating in the run, whereas the readout process starts after a Level-2 trigger. Between triggers, the data stream is processed by the digital filter circuits and then stored temporarily in a buffer. When the Level-2 trigger is received, this data is frozen in memory and shipped to the data acquisition system. Otherwise the data is overwritten. This process defines two contributions to the dead-time generated by the TPC: detector dead time, i.e. the drift time, and the FEE dead time (event readout time). Whenever the TPC cannot process any further events, a signal (busy signal) is asserted to prevent the CTP from issuing subsequent triggers.

3.2 Choice of the Gas and Gas System

Choice of the mixture: The gas mixture of the ALICE TPC is ideally expected to provide saturated high electron drift velocity, low electron diffusion, high gain and resolution,

high ionisation rate, high stability, large ion mobility, low Z and low dependence to the external parameters. But unfortunately it is impossible to handle all those requirements at the same time. Therefore an optimization process had to be carried out.

The selection of the main gas component and the quencher was made by a process of elimination rather than choosing the gas by its merits. The resulting candidates for the ALICE TPC, on grounds of ageing, inflammability, toxicity, neutron capture, density and price, are Argon, Neon and CO_2. But none of them is satisfactory as sole ingredient in view of operational stability, drift velocity and diffusion. Therefore a mixture, such that Argon or Neon nobel gases as main component and CO_2 as the quencher, was chosen [36].

The expected high multiplicities with high rates of secondary particles and the required momentum resolution rule out the use of Argon. The Argon based mixtures have higher number of ionization ions per unit length and a lower ion mobility. These ions, a factor of 3 slower than the ions in Neon, enhance the space-charge effect and thus lead to sizeable field distortions and spatial corrections of the order of 1 mm. The noble gas, hence, must be Neon.

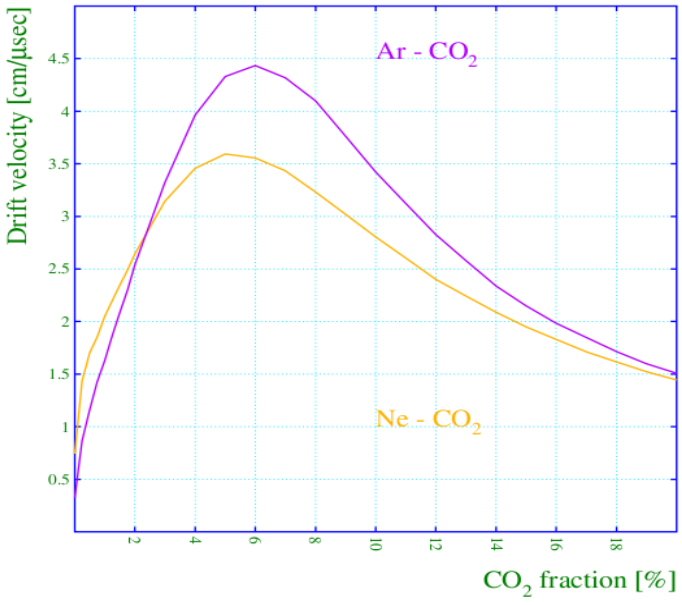

Figure 3.5: *CO_2 dependence of the relative change of the drift velocity for the Ne-CO_2 and Ar-CO_2 gas mixtures [36].*

Adding CO_2 reduces the transverse diffusion due to its large electron scattering cross section. This results in an increase in the drift velocity up to a CO_2 fraction of about 6% and then a decrease as seen in Fig. 3.5. Additionally, high electron attachment coefficient of CO_2 in the amplification region and maximum tolerable drift time of 92 μs with nominal drift field 400 V/cm leads to a maximum CO_2 concentration of 10% [36].

Further, it was decided to add $\sim 5\%$ N_2 to the mixture [34]. This addition reduces the drift velocity at the nominal field by about 5% (Fig. 3.6), but it improves the stability of the readout chambers which are operated at a relatively high gain of $\sim 2 \times 10^{-4}$ (Fig. 3.7). Moreover, N_2 supports CO_2 as a quencher by reducing the undesirable Penning effect [36] in the avalanche.

Taking everything into account, the resulting gas mixture Ne-CO_2-N_2 (85.7%-9.5%-4.8%) satisfies most of the requirements of the ALICE TPC such as low diffusion, low Z, large ion

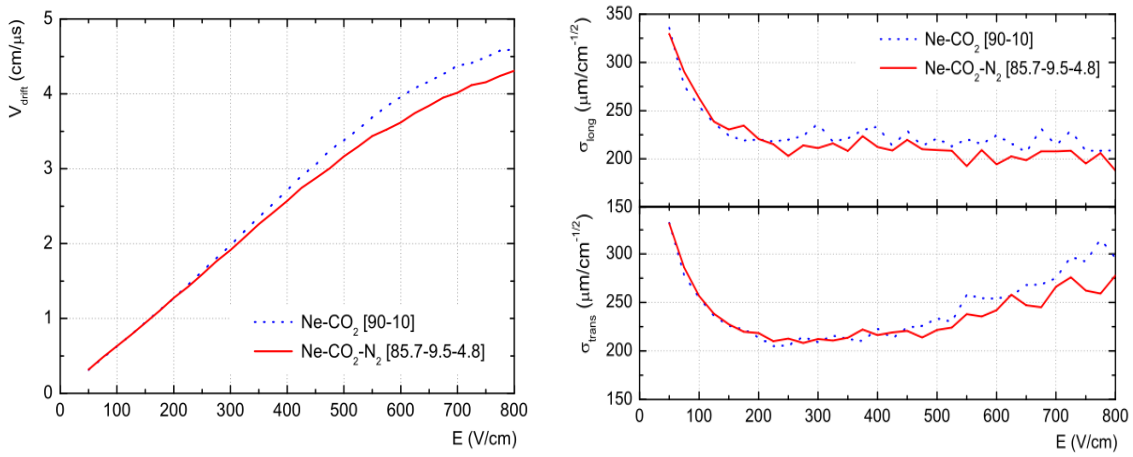

Figure 3.6: *Drift velocity (left) and longitudinal and transverse diffusion coefficients (right) as a function of the electric field for the Ne-CO_2 (dashed lines) and the Ne-CO_2-N_2 (solid lines) mixtures calculated with Magboltz at 750 Torr and 20°C [15].*

mobility, higher operational stability of the readout chambers and high gain. Nevertheless, owing to the non saturated drift velocity in the TPC, the exact composition of the gas needs to be monitored carefully.

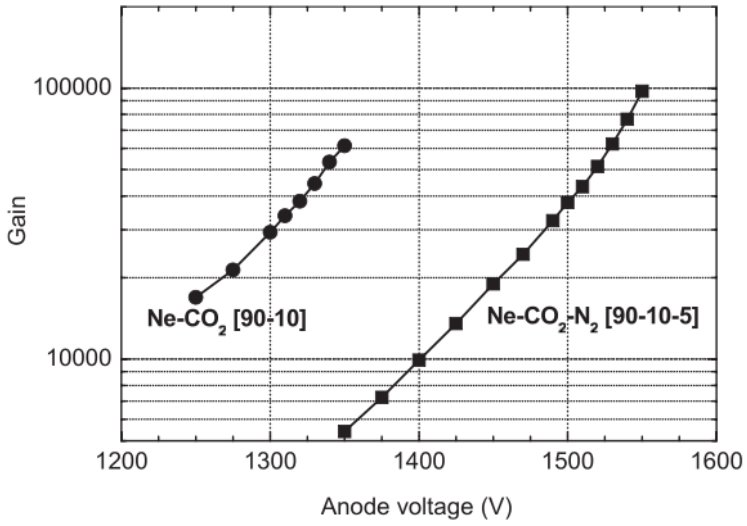

Figure 3.7: *Comparison of gas gain as a function of the anode wire voltage for a Ne-CO_2 and a Ne-CO_2-N_2 gas mixture [34].*

Gas System: TPC uses a recirculating gas system due to its large volume [15]. This makes the external gases, mainly N_2, O_2 and H_2O, mix in the system indispensable. Since O_2 and H_2O have the very unfavourable effect of causing electron attachment, they have to be removed from the gas. This is done by routing the recirculated gas through a purging station which uses activated copper and a molecular sieve to remove these two components. The monitoring and cleaning of these contaminations are done regularly.

3.3 Cooling and Temperature Monitoring System

The required temperature stability and homogeneity within the TPC drift volume is less than 0.1 K in order to achieve the desired resolution in the drift direction. The temperature monitoring and cooling systems were therefore designed in order to maintain a precise control of thermal influences on the sensitive volume of the TPC. Important heat sources affecting the TPC are the FECs, which are connected to the cathode pad plane of the ROCs, the power produced by the bus bars, four field cage resistor rods and the adjacent detectors ITS and TRD.

To monitor the temperature distribution of the TPC, 496 PT1000 sensors are mounted both inside and outside of the gas volume of the TPC to measure the temperature with an accuracy better than 50 mK (Fig. 3.8). Several sensors (2×18) are attached to a circular skirt inside the gas volume. In addition to the sensors covering the outside of the Inner and Outer Field Cage containment vessels, several sensors are mounted onto each ROC. For each sector, sensors measure the cooling water inlet and outlet temperature. There are also heat-screens towards the other detectors and the environment. Additional temperature sensors on the front-end electronic cards complete the monitoring system [15, 37].

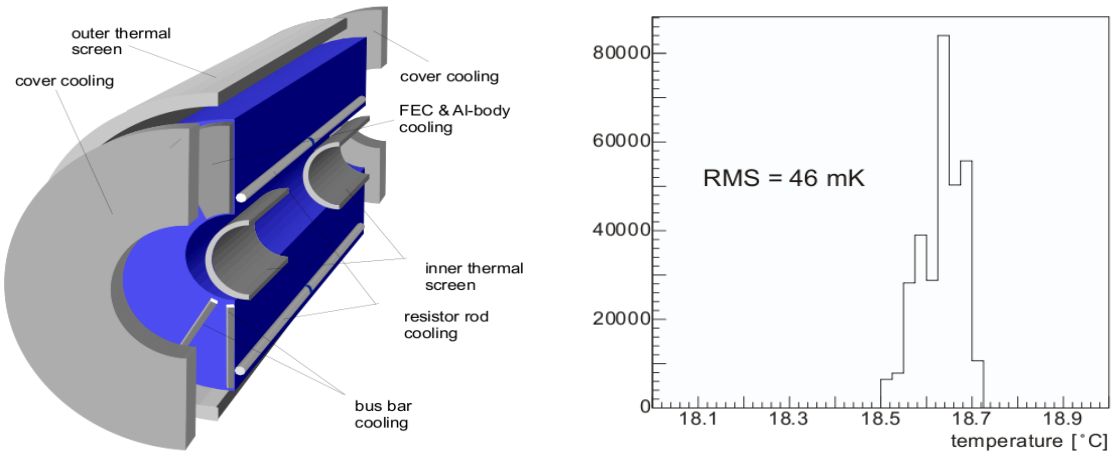

Figure 3.8: *Schematic view of the various TPC cooling elements (left). Temperatures distribution measured with the skirt PT1000 sensors (right) [15].*

Cooling and temperature stabilization of the heat sources is provided by means of 60 individual water-cooling loops which are supplied by three different cooling plants. All loops are independent from each other in the sense that the flow and the temperature can be regulated independently [38, 39].

3.4 Physical Processes in the TPC

3.4.1 Gas Ionization and Energy Loss

A charged particle that traverses the gas in the TPC leaves a track of ionization along its flight path. The TPC provides a complete 3D picture of the ionization deposited in the chamber. The energy required for the ionisation is taken from its kinetic energy and is typically a few keV per centimeter of gas in normal conditions. The density of the ionization, along the track, depends on the momentum and type of the particle.

Under the influence of the electric field, ionization electrons drift to either of the two endplates and are amplified at the wires in avalanches. The electrical signal, obtained by means of the gas amplification, allows the readout electronics to provide the projection of the track. Together with an accurate measurement of the drift time of the electron clusters, with respect to some external reference such as the collision time, a reconstruction software calculates the origin of the ionisation as three dimensional space points. Afterwards, the complete trajectory of the particle can be determined with precision from the reconstructed space points by a tracking algorithm. Because of the applied magnetic field parallel to the E field inside the TPC, the actual path of the charged particle is bent according to its charge and momentum. The momentum can then be deduced from the bending radius of the particle trajectory. Finally, together with the known momentum, the measurement of the mean energy loss per track length $\langle dE/dx \rangle$ allows for the particle identification.

The energy loss per unit of pathlength due to coulomb interactions is given by the Bethe-Bloch approximation which describes the integral over all the energies lost to the individual atoms of the medium in the framework of relativistic quantum theory of collisions.

$$\left\langle \frac{dE}{dx} \right\rangle = \frac{4\pi N\rho}{mc^2} \frac{Z}{A} \frac{1}{\beta^2} \left(\ln \frac{2mc^2}{I} \beta^2\gamma^2 - \beta^2 - \frac{\delta(\beta)}{2} \right), \tag{3.1}$$

where; mc^2 is the rest energy of electron, e is the elementary charge, z is the charge of the travelling particle, β is the velocity of the travelling particle in terms of the speed of light, γ is the Lorentz factor, N is Avagadro number, Z, A are the atomic number, mass of the medium, ρ is the gas density, I is the mean excitation energy of the atom calculated by using the Thomas-Fermi theory of the atom and $\delta(\beta)$ is the correction term [28, 40].

3.4.2 Electron Drift and Diffusion

Electron Drift: In microscopic level, an electron scatters isotropically with an instantaneous velocity ν immediately after the collision [40]. However, some short time later, it picks up the extra velocity u, which appears macroscopically as the drift velocity, equal to its acceleration along the field. In this sense, the drift of the electrons under the influence of an electric and a magnetic field is given by an equation of motion:

$$m\frac{d\mathbf{u}}{dt} = eE + e\left[\mathbf{u} \times \mathbf{B}\right] - K\mathbf{u}, \tag{3.2}$$

where m and e are the mass and charge of the electron and $K\mathbf{u}$ is the friction term. The ratio m/K has the dimension of a characteristic time and can be interpreted as the average time between collisions τ:

$$\tau = \frac{m}{K}. \tag{3.3}$$

In view of the fact that $t \gg \tau$, the drift velocity is taken to be constant i.e $du/dt = 0$. Thus, equation (3.2) gives:

$$\frac{\mathbf{u}}{\tau}\frac{e}{m} - \left[\mathbf{u} \times \mathbf{B}\right] = \frac{e}{m}\mathbf{E}. \tag{3.4}$$

From here, introducing the cyclotron frequency $\omega_x = (e/m)B_x$ and $\varepsilon_x = (e/m)E_x$ etc.

One can conclude the drift velocity u as:

$$u = \frac{e}{m}\tau|E|\frac{1}{1+\omega^2\tau^2}\left(\mathbf{e} + \omega\tau\left[\mathbf{e}\times\mathbf{b}\right] + \omega^2\tau^2\left(\mathbf{e}\cdot\mathbf{b}\right)\mathbf{b}\right), \tag{3.5}$$

where $\mathbf{e}$ and $\mathbf{b}$ denote the unit vectors in the direction of the electric and magnetic fields respectively. The drift direction is governed by the dimensionless parameter $\omega\tau$. For $\omega\tau = 0$, the drift velocity is along the electric field. In this case the relation has the simple form:

$$\mathbf{u} = \frac{e}{m}\tau\mathbf{E} = \mu\mathbf{E}, \tag{3.6}$$

$$\mu = \frac{e}{m}\tau, \tag{3.7}$$

where μ is the scalar electron mobility.

Diffusion: As the drifting electrons are scattered on the gas molecules, their drift velocity deviates from the average due to the random nature of the collisions. In the absence of electromagnetic fields, the deviation is the same in all directions, and a point-like electron cloud starting to diffuse at time $t = 0$ from the origin in the z direction will, after some time t, assume the following Gaussian density distribution:

$$n = \left(\frac{1}{\sqrt{4\pi Dt}}\right)^3 \exp\left(-\frac{r^2}{4Dt}\right), \tag{3.8}$$

where r is the distance to the origin; $(r^2 = x^2 + y^2 + (z - ut)^2)$ and D is the diffusion constant because n satisfies the continuity equation for the conserved electron current [40]. The electric field, however, breaks the isotropy in such a way that the diffusion in drift direction and perpendicular to it are different. Hence, equation (3.8) has the form:

$$n = \left(\frac{1}{\sqrt{4\pi D_l t}}\right)\left(\frac{1}{\sqrt{4\pi D_t t}}\right)^2 \exp\left[-\frac{x^2+y^2}{4D_t t} - \frac{(z-ut)^2}{4D_l t}\right], \tag{3.9}$$

where D_l and D_t denote the two different diffusion constants in longitudinal and transverse direction. Equation (3.8) shows that the width of the density distribution σ is given by $\sigma^2 = 2Dt$. Together with $L = ut$, the width can be written as:

$$\sigma^2 = \frac{2D}{u}L, \tag{3.10}$$

where t is the drift time of the electrons and L the length travelled during that time. However, as a characteristic measure for the diffusion in a gas, the drift length independent

quantities:

$$D_L = \frac{\sigma_l}{\sqrt{L}} = \sqrt{\frac{2D_l}{\mu E}} \tag{3.11}$$

$$D_T = \frac{\sigma_t}{\sqrt{L}} = \sqrt{\frac{2D_t}{\mu E}} \tag{3.12}$$

derived from equation (3.6) and (3.10), are used [28].

3.4.3 Signal Creation

As the drift electrons approach the vicinity of the anode wires, they encounter an electric field increasing with the decreasing distance to the wires. After some point, the energy gained by the electrons between collisions becomes so large that they ionise the gas, producing secondary electrons. This causes an avalanche to start and the initial charge is amplified by a factor of about several thousands depending on the anode high voltage.

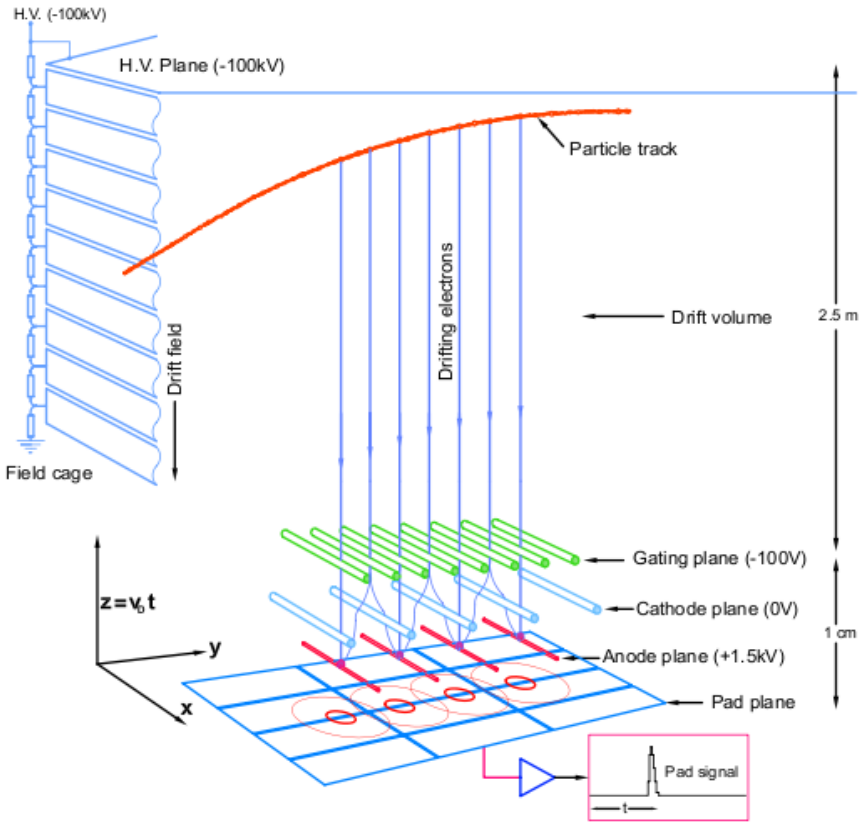

Figure 3.9: *Schematic illustration of the working principle of TPC [41].*

The amplification region is defined by the cathode wires, anode wires and the pad plane (Fig. 3.9). The gating grid is located between the cathode wires and the drift region to prevent positive ions, generated in the amplification process, to drift back into the drift volume and create field distortions. The anode wire voltage is chosen such that the produced signal is proportional to the original charge. The proportionality is given as long as

the field of the produced ions is negligible compared to that of the wire.

The gating grid works between two modes; closed and open. In the open gate mode, all gating grid wires are held at the same potential V_g, which is defined by the potential of the drift field at the place of the gating grid. In this case, the grid is transparent to charge transport between amplification and drift regions. Therefore the gating grid is closed by default and only opened in case of a triggered event. The opening duration is given by the drift time over the full TPC length ~ 92 μs. In the closed gate mode a voltage of $V_g \pm \Delta V$ is applied to alternating wires. The necessary value of ΔV, which is given by the magnetic field, the wire spacing, and the drift field, is ± 90 V. Further, a gate pulser system has been devised to enable the rapid transition of the gating grid from the 'closed' to the 'open' mode upon the receipt of a trigger [15].

On the other hand, UV photons are also produced in the avalanche. A fraction of these photons are energetic enough to ionise the gas. This results in some additional undesired ionisations in the gas and the photo electrons in the cathode plane. This effect is removed by the quench gases (CO_2-N_2 see section..) which have a large number of rotational and vibrational modes i.e. large photoabsorption coefficients.

The ions produced in the amplification process are collected at the cathode wires and the secondary electrons with about 1000 times larger drift velocity of the primaries at the anode wires. The field of the ions induces a mirror charge on the pads which creates the pad signal. The wire geometry is chosen such that on average the signal spreads over three adjacent pads. Determining the center of gravity of the charge distribution, a position resolution much better than the actual pad size is achieved. Lastly, the signal is amplified and shaped by the FEE of the TPC.

3.4.4 Two Photon Ionization

Laser beams are used to produce ionisation tracks in the active volume of the TPC for calibration and surveying purposes (See Section 4.2). The pulsed UV laser used has a wavelength of 266 nm which corresponds to the energy of 4.66 eV. However, the molecules taking part in the ionisation process are not the basic components of the gas mixture (Ne, CO_2, N_2) but organic impurities in the gas with the ionisation potentials of $5-8$ eV. Further, the cross section for $3-4$ photon ionisation is extremely low. The ionisation process with the lasers, therefore, is dominated by the two photon process.

Relevant processes are given in Fig. 3.10. The most dominant ones being probably B and also D, if the singlet to triplet transition rate $S_1 \rightarrow T_1$ is high. The stimulated transitions from one state to another are proportional to the incoming photon flux, where the constant of proportionality is the corresponding transition cross-sections [42].

Assuming recombinations are negligible, the physics process is described with the following differential equation system;

$$\frac{dn_i}{dt} = n_e \sigma^* N, \tag{3.13}$$

$$\frac{dn_e}{dt} = (n_0 - n_e)\,\sigma_e N - n_e \sigma_i^* N - n_e/\tau, \tag{3.14}$$

where N is photon flux (photon/cm^{2}s), τ is the life time, σ is cross-section, $n_0, n_e(t), n_i(t)$ are molecule densities of ground, exited and ionized states, respectively. Integration of

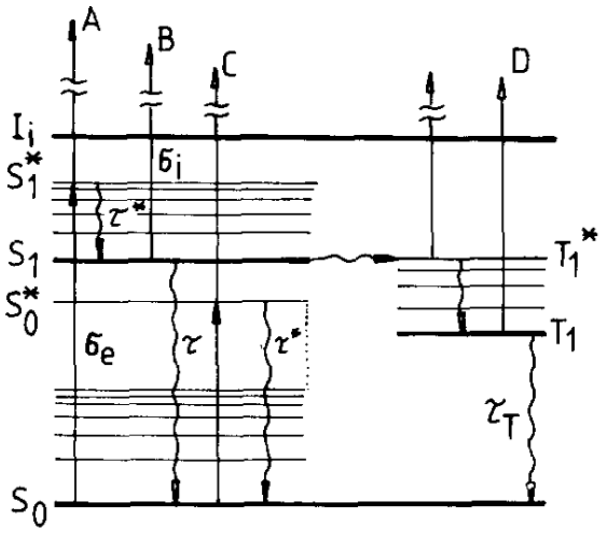

Figure 3.10: *Schematic energy level diagram of complex molecule, indicating possible channels for 2-photon ionisation [42].*

these equations gives;

$$n_e(t) = \frac{a}{b}\left(1 - e^{-bt}\right), \tag{3.15}$$

$$n_i(t) = \sigma_i^* N \frac{a}{b}\left(T + \frac{1}{b}(e^{-bT} - 1)\right), \tag{3.16}$$

where T is the width of the laser pulse, $a = n_0\sigma_e N$ and $b = (1/\tau + \sigma_e N + \sigma_i^* N)$. Assuming N is constant, this leads to

$$n_i\,(T) = n_0\sigma_e\sigma_i^* N^2 \frac{T}{b}\left[1 - \frac{1}{bT}\left(1 - e^{-bT}\right)\right]. \tag{3.17}$$

For the limiting case of low photon flux and long lifetime of the intermediate state τ $\left(\gg T \sim 10^{-9}s\right)$ i.e. $bT \ll 1$, equation (3.17) yields:

$$n_i\,(T) = \frac{1}{2} n_0\sigma_e\sigma_i^* N^2 T^2. \tag{3.18}$$

As a conclusion, the ionization density is proportional to the square of the photon flux N^2. That means, it is crucial that the laser intensity is stable in order to get a constant ionisation rate, which is required to use the lasers as a calibration tool [40, 28].

4 Online Drift Velocity Calibration with the TPC Laser System

4.1 Drift Velocity Calibration

4.1.1 Importance of the Drift Velocity Calibration

Precise reconstruction of particle tracks in the TPC requires a thorough understanding of the drift velocity. The drift velocity, in conjunction with the drift time measured by the FEE, provides the z position information of the particles traversing the TPC volume. Thus, together with the xy projection of the ionization point, it builds up the three dimensional space point which is the starting point of the track finding in the TPC. Drift velocity calibration, therefore, is very fundamental and crucial for tracking and particle identification.

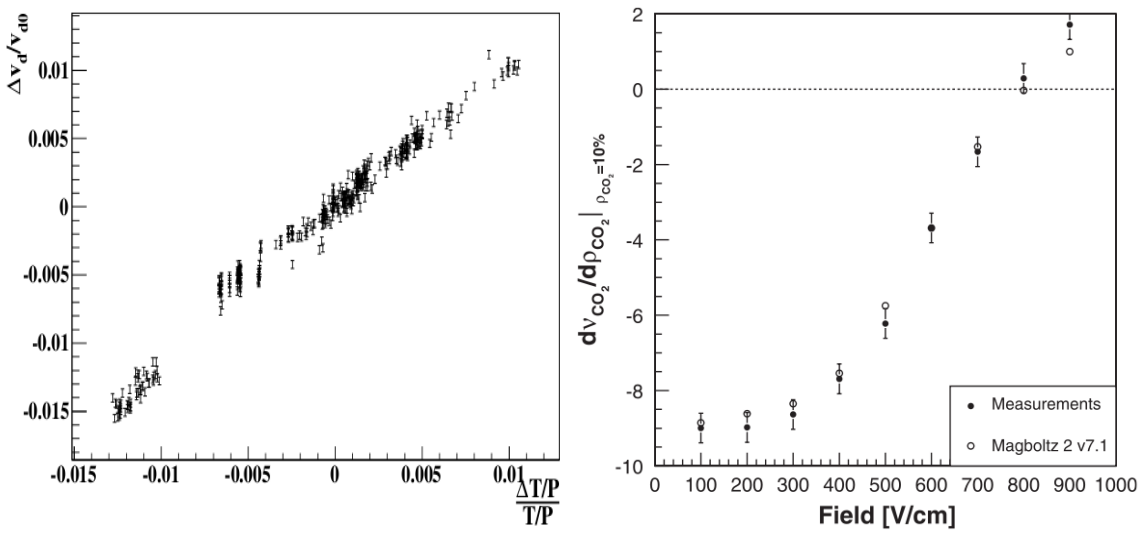

Figure 4.1: *Drift velocity variation in Ne-CO_2 (90%-10%) as a function of $\Delta(T/P)$ (left). CO_2 dependence of the drift velocity around 10% CO_2 as a function of the electric field (right) [36, 43].*

In section 3, it was shown that the drift velocity is a function of the electromagnetic fields and the mobility. The mobility depends on the gas density which is a function of the environment variables as well as the gas composition. The drift velocity, therefore, changes in time as a function of many parameters [15]:

$$u = u\left(E, B, N\left(P, T\right), C_{CO_2}, C_{N_2}\right), \tag{4.1}$$

where E and B are the electric and magnetic fields, N is the gas density, P and T are the pressure and temperature inside the TPC and C_{CO_2} and C_{N_2} are the concentrations of CO_2

and N_2. A significant change of the drift velocity due to changes in the gas composition as well as E and B field variations has a time constant of several hours, while the changes due to pressure and temperature variations have to be corrected on the level of minutes.

Pressure and temperature variations affect the drift velocity only in that they both modify the density. Under nominal conditions, i.e. $E = 400$ V/cm, room temperature (~ 300 K) and atmospheric pressure (~ 1013.25 mbar), the drift velocity has a sensitivity to temperature variations of about 0.35% per Kelvin (Fig. 4.1). In order to limit the temperature induced distortions to 1 mm over the maximum drift path of 250 cm , one therefore needs to stabilize the temperature to 0.1 K. In terms of pressure, 1 mm distortion in the drift direction corresponds to about 0.4 mbar. Pressure changes are easier to correct compared to temperature changes [36].

With 10% CO_2 and a drift field of $E = 400$ V/cm the drift velocity is reduced by 7.7% per percent of CO_2 (Fig. 4.1) and the addition of $\sim 5\%$ N_2 reduces the drift velocity by about 5% (See Fig. 3.6) [15]. Since the gas mixture is likely to be uniform over the entire volume as well as reasonably stable in time, mixture induced errors are less harmful than the more localized temperature induced errors.

All in all, an elaborate calibration of the drift velocity is crucial to achieve the required drift velocity resolution of the order 10^{-4}, which results from considering a space point resolution of 200 μm over the full drift length of 250 cm.

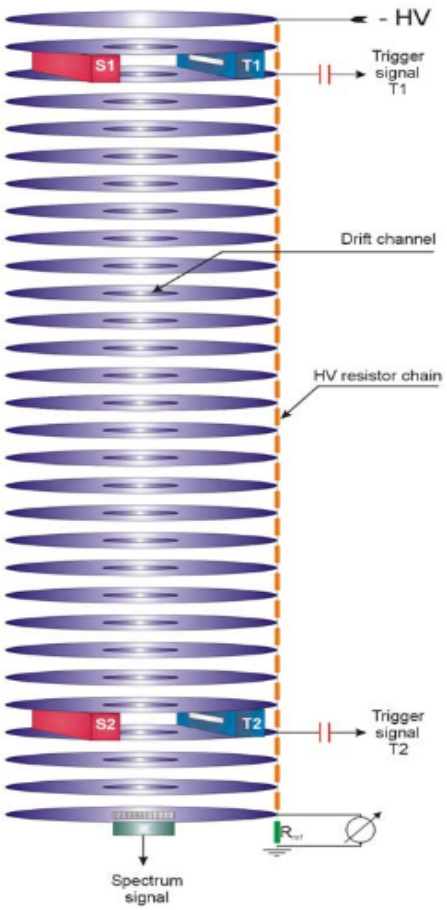

Figure 4.2: *Schematic view of Goofie [9].*

4.1.2 Drift Velocity Calibration Methods being used in the ALICE-TPC

The main goal of the drift velocity calibration is to retrieve the required drift velocity correction parameters to be used in the offline software which handles the reconstruction process. In addition to the online method using the laser system, which is the main theme of this thesis, the following methods are being used for the drift velocity calibration. The methods can be combined to increase the accuracy.

4.1.2.1 Online Gas Monitoring System 'Goofie'

The Goofie [9] is an online gas monitoring system used to monitor the gas gain and the drift velocity. Using these information, it also calculates the gas composition. The schematic view of the drift velocity monitor is shown in Fig. 4.2.

The principle of operation of the drift velocity monitor is based on the measurement of the difference in the drift time of electrons, produced through the ionization tracks of α-particles, at two known distances from a so-called pick-up electrode. Two counters (T_1, T_2) facing each an alpha source (S_1, S_2) provide the trigger signal. The electrons released in the gas drift down to the pickup detector through the constant field of 400 V/cm. The drift velocity is extracted from the position in time of the peaks corresponding to the signals coming from both the near and the far source.

4.1.2.2 Offline Methods

As discussed in section 4.1.1, the drift velocity depends on many parameters. The first order taylor expansion of these dependencies around the nominal values is [15]:

$$\Delta u = u - u_0 = \frac{du}{dE}\Delta E + \frac{du}{dN}\Delta N(P,T) + \frac{du}{dC_{CO_2}}\Delta C_{CO_2} + \frac{du}{dC_{N_2}}\Delta C_{N_2}. \tag{4.2}$$

Since the changes due to the pressure and temperature variations are efficient on the level of minutes, whereas the others are several hours, the influence of the T and P are prioritized. Therefore, the correction factor x is given with the following formula:

$$x = \frac{\Delta u}{u_0} = k_0(t) + k_N\frac{\Delta N(P,T)}{N_0(P,T)} = k_0(t) + k_{P/T}\frac{\Delta(P/T)}{(P/T)_0}, \tag{4.3}$$

where the influence of the gas composion and electric field changes are summarized under the time dependent offset factor $k_0(t)$.

The offline drift velocity calibration techniques use the reconstructed track information of the physics tracks, as well as the laser tracks provided by the laser calibration system. They measure the correction factor x with the following approaches:

- matching laser tracks with the surveyed mirror positions,
- matching TPC tracks with the ITS tracks,
- matching of the TPC primary vertices from the two halves of the TPC,
- matching tracks from two halves of the TPC using cosmic tracks.

The unknown parameters $k_0(t)$ and $k_{P/T}$ are determined using a Kalman filter approach.

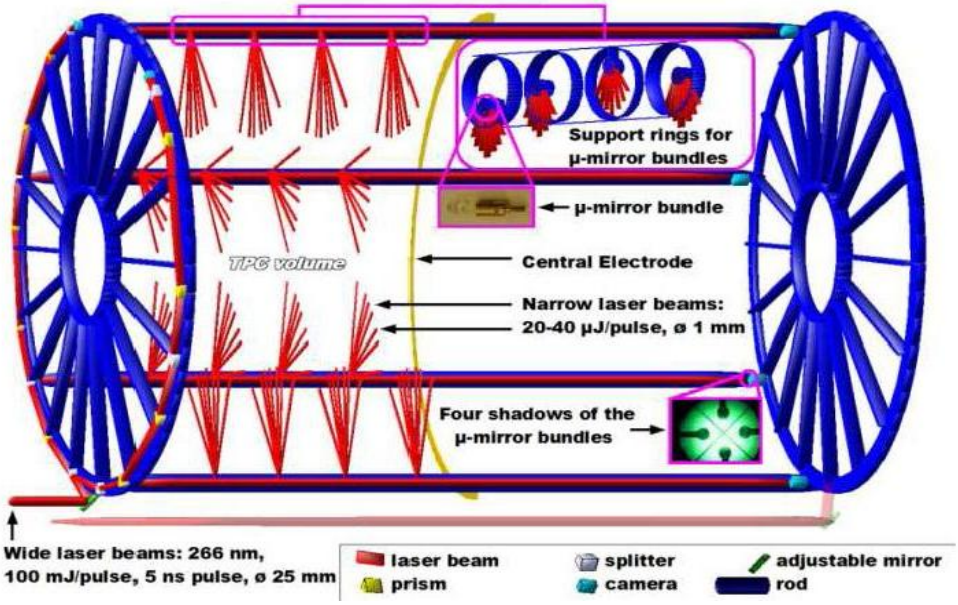

Figure 4.3: *Schematic 3D view of the TPC and the laser system.*

4.2 TPC Laser System

UV lasers are powerful tools for calibration and surveying of drift chambers and for precision measurements of electron transport parameters in gases. The principal advantages of UV lasers for the production of ionization tracks in gases are [42]:

- Cheap, transportable and flexible test beam setup.
- Good resolution in space and time over several meters: no production of γ-rays, no multiple scattering.
- No curvature in magnetic fields.
- Ionization density controllable with small fluctuations.
- Ideal tool for two-track studies, e.g. via simple beam reflection.

For these reasons a laser system was constructed for the ALICE-TPC as a versatile tool for calibration purposes. In this section, the layout and the elements of the system are described in some detail.

4.2.1 The Layout of the TPC Laser System

The laser system is used to generate straight tracks, similar to ionizing particle tracks, at known positions in the drift volume of the TPC [44]. An overview of the system is shown in Fig. 4.3.

In total 336 tracks are generated by two-photon ionization (section 3.4.4) of the drift gas. For this a pulsed UV laser beam with a wavelength of 266 nm, which is obtained from a Nd:YAG laser (1064 nm), is used [45]. This wavelength corresponds to the energy of $E = h\nu = 4.66$ eV. Most metallic surfaces have work functions below 4.66 eV. Therefore, a considerable amount of low energy photo-electrons are expected from the central electrode

(CE) synchronously with the laser pulse. After a characteristic drift time, nearly each of the 557568 readout pads receives this signal.

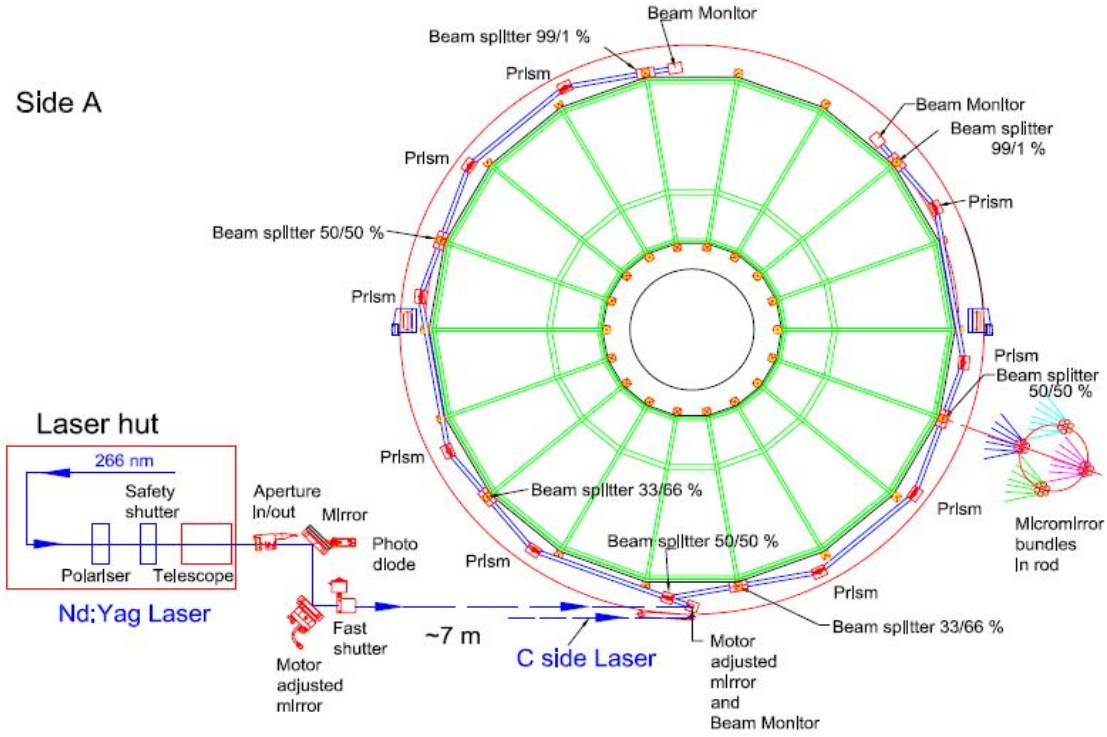

Figure 4.4: *Overview of the optical elements to guide the laser beam from the laser hut to the entrance windows in the TPC field cage. The A side system is shown. The C side system is obtained by mirror symmetry in a vertical plane along the TPC axis [15].*

The reconstructed laser tracks, together with the CE signal, are used for the calibration of the electronics, alignment of the ROCs, studying field distortions and $E \times B$ effects, gain and drift velocity calibration [44].

4.2.2 Generation and Distribution of Laser Beams

The basic principle of generating hundreds of narrow laser beams simultaneously in the TPC volume was developed for the STAR experiment at RHIC [46] and has been modified appropriately for ALICE.

The ALICE-TPC laser calibration system is composed of a static optical system with a few adjustable parts. The static optics is composed of beam splitters, mirrors and bending prisms guiding the laser beam before it enters the TPC volume. The guiding system ends with cameras for the purpose of monitoring the position and intensity of the remaining beams. This information is used for the alignment of the adjustable part of the system. The adjustable part is mainly composed of remotely controllable mirrors that guide the beam into the static optical system.

The laser is placed in a hut outside the L3 magnet at a distance of 10 m to the TPC (Fig. 4.4). It is specified to provide 100 mJ/pulse of 5 ns duration and 266 nm wavelength at a repetition rate of 10 Hz. Built into the laser is also a beam expanding telescope to

enlarge the beam diameter from $9 - 10$ mm to 25 mm and reduce the beam divergence to approximately 0.3 mrad. Close to the laser, the beam has a flat intensity profile across the beam spot which develops smoothly into a gaussian profile after $20 - 30$ m.

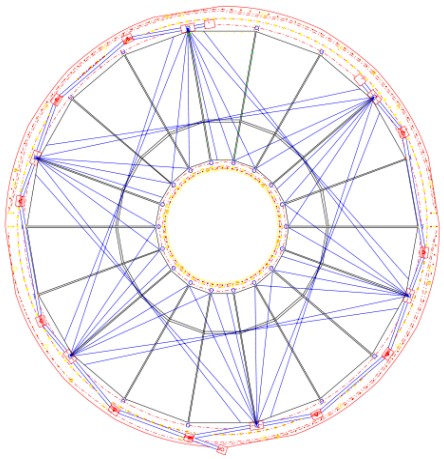

Figure 4.5: *Ideal laser tracks projected to the endcap. The pattern repeats eight times through the full length of the TPC.*

From the laser hut, two wide laser beams exit horizontally. One beam is guided to the A-side end-plate close to its outer radius, where a mirror reflects it by 90° into a vertical plane parallel to the TPC end-plate. The other beam passes slightly lower and continues in a straight line to the C-side end-plate where likewise another 90° mirror bends it into the vertical plane parallel to this plate. After the beam is reflected into the vertical plane at the bottom of the TPC, a 50% beam splitter directs half of the beam in each direction to the laser rods, as shown in Fig. 4.4. The beam paths at the two TPC ends are virtually identical, except that one of the prisms on the C-side has a smaller bending angle to compensate for the beam entrance shift of 10° in ϕ.

The wide beams travel along the inside of the rods as illustrated in Fig. 4.6 and are intersected by four micro-mirror bundles before arriving at the TPC central electrode at $z = 0$. Here, the undeflected part of the wide beam goes through an empty gas rod in the other half of the TPC. At the far end, the beam position and intensity are monitored by a camera, using the Poisson Spot technique [45].

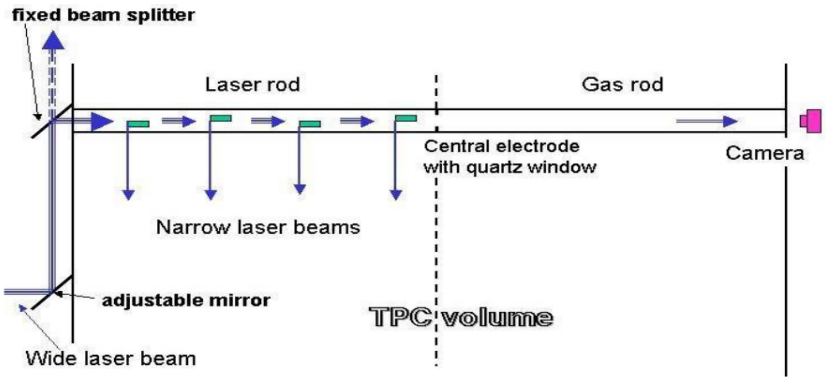

Figure 4.6: *Principle of generating narrow laser rays in the TPC volume [45].*

The wide beams hit bundles of seven one-millimeter diameter micromirrors. The narrow beams spread out from these bundles roughly in a plane perpendicular to the wide laser beam and were rotated along their axis to give predefined azimuthal reflection angles: $2,5°$, $\pm 9,2°$, $\pm 16°$ and $\pm 31,8°$, as shown in Fig. 4.7. The angles were optimized such that the narrow beams cross the sector boundaries strategically, i.e. at points where alignment between sectors would benefit the most. A projection on the transverse-plane of the starlike pattern of laser rays is shown in Fig. 4.5.

Furthermore, beams from neighboring laser rods in ϕ are shifted slightly in z relative to each other to avoid most of the apparent beam crossings. The micro-mirror bundles, thereby, are positioned at $z = \pm 130, 850, 1690, 2470$ mm for odd laser rods and $z = \pm 100, 790, 1630, 2410$ mm for even rods [44].

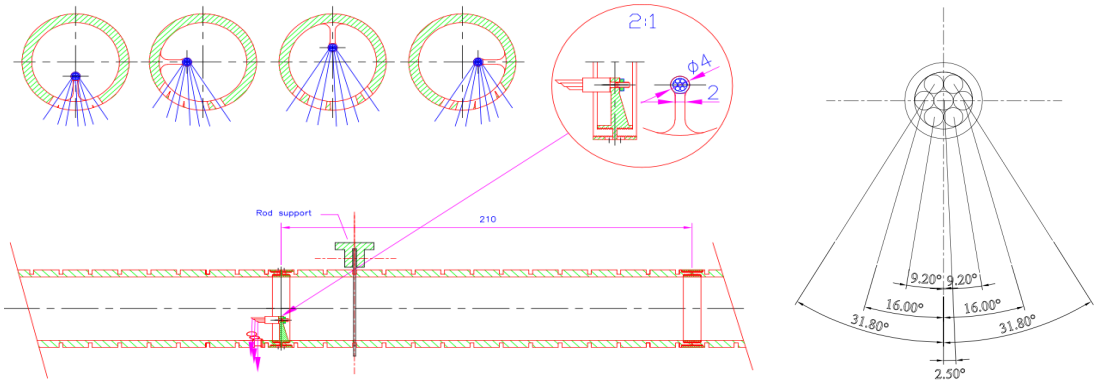

Figure 4.7: *Laser rod with micro-mirror bundle and its support, as well as the position of four mirror bundles (left). Azimuthal reflection angles of each mirror bundle (right) [45].*

4.2.3 Spatial Precision and Stability

The TPC calibration with laser tracks requires the knowledge of the ideal spacial position of all laser tracks. Given the mechanical tolerances, the best absolute coordinate frame for each half of the TPC is defined by the plane of the end plate. All ROCs and the plane of the CE were aligned and adjusted relative to the end plates.

In order to obtain a relative electric drift field error below 5×10^{-4}, these surfaces, as well as the 4 laser track planes on each side, were defined relative to each other to a precision of approximately 100 μm. A final precision goal of $800 - 1000$ μm for space points translate to the following requirements on spacial coordinates and angles of the laser system: $(\triangle x, \triangle y, \triangle z) \leq 800 - 1000$ μm, $(\triangle \varphi, \triangle \phi) \leq 0.4 - 0.5$ mrad [15].

The most important issue in the definition of the laser track positions is the placement of the micro-mirrors. The mechanical construction errors of the micro-mirror bundles are specified to be less than 100 μm in the spacial measures and less than 1° in all reflection angles. This production tolerance of 1° results in deviations of up to 40 mm near the inner cylinder [45]. The only other deviation from the ideal rays that matters is the incidence angle of the wide laser beams on the micro-mirrors which is relatively easy to measure and keep constant due to the long lever arms in the optics system.

4.2.4 Data Taking

The data taking system of ALICE is designed to take data in various run configurations, either in dedicated calibration runs with laser triggered events only or in a mode where the laser events are interspersed between physics events.

For stand-alone calibration runs, a fixed total number of events (typically 1000-5000) is recorded. In case of physics runs, a set of laser events, a so-called "burst", with a fixed number of events (e.g. 100 events) are interleaved between physics triggers. After one burst is taken, the laser is put into a standby mode for a period of about 1 hour. Therefore, depending on the length of the run, one run can include more than one burst. This burst mode of operation is handled automatically by the DCS and is designed to ensure a reasonably long laser flashlamp lifetime [44].

4.3 Online Drift Velocity Calibration Method

The main goal of the online drift velocity calibration is to provide calibration parameters required at the very beginning of the offline reconstruction process. Since the main part of the reconstruction is combined track finding (see section 2.4), a good track matching efficiency between the detectors is crucial. Therefore, the drift velocity has to be measured with a good precision before the combined track finding process in order to determine the z position of the particle tracks with sufficient accuracy.

In this sense, it was aimed to develop a drift velocity calibration method which provides start values to be used in the first reconstruction pass. The overall description of the method is given in the following:

4.3.1 Data Filling

During the analysis raw data in root format was used as an input, whereas at the online stage the DATE format will be used. After the selection of laser triggered events, the digits of all events summed up within one burst were filled into a multidimensional histogram (see section 4.2.4). This histogram contains the digit information (sector, row, pad, time bin) and the ADC values, as well as the time stamp (i.e. event time). The data processing was done iteratively for each burst i.e. a burst by bust study was performed.

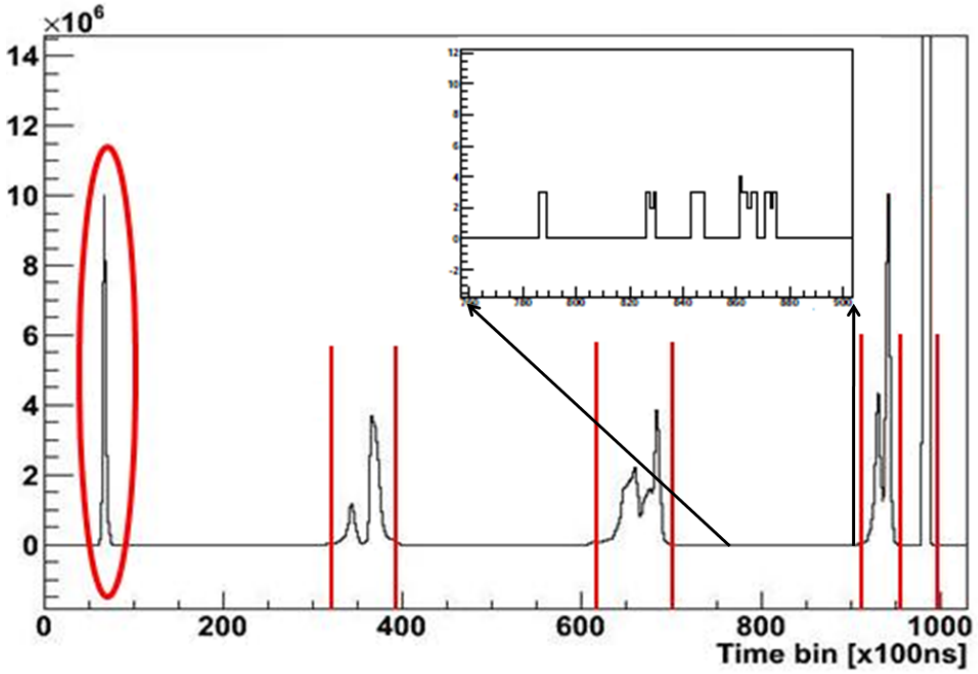

Figure 4.8: *The projection of the ADC counts on the time bin axis. Red lines indicate the cut windows applied and the circle the excluded first laser plane. The inset shows the noise signals within the selected window.*

The online processing of the raw data over all the TPC pads is very demanding in terms of cpu time and memory consumption. Therefore, in order to reduce the data size and also to remove most of the noise signals and part of the data, which is affected by significant distortions, some cuts were applied at the stage of data filling:

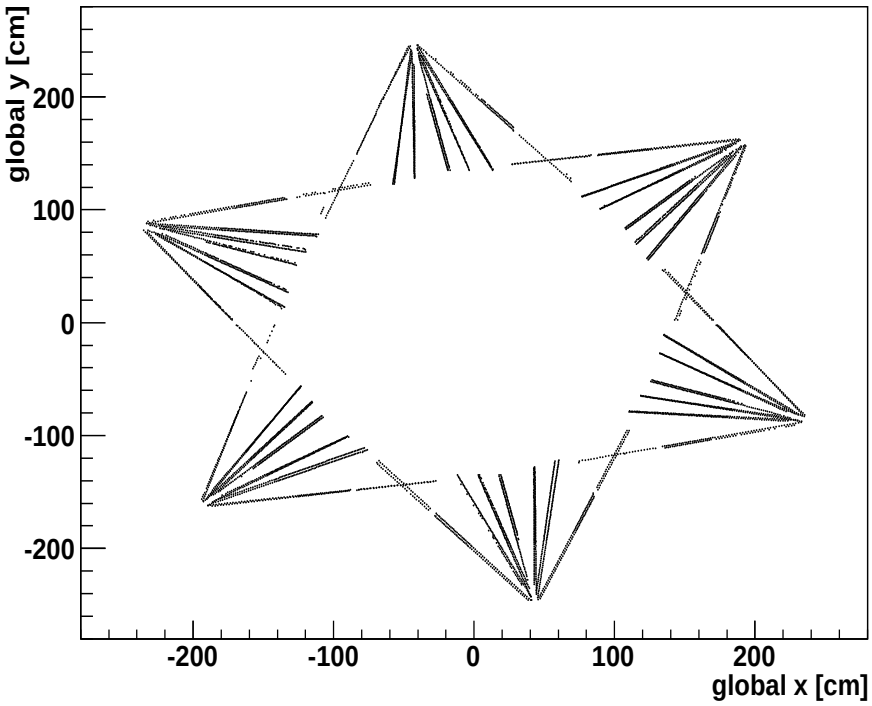

Figure 4.9: *The projection of the A-Side laser tracks on the xy plane, after the exclusion of IROCs*

First, the laser track signals on the IROC pads were excluded. Those tracks are more distorted for several reasons: The angular uncertainties play a significant role in this region (see section 4.2.3). Due to the fact that IROCs are far away from the micro-mirror bundles, these regions may have tracks with low intensity. Further, the different geometries of the IROC and OROC require some additional corrections (e.g. IROC-OROC alignment) to be taken into account. Consequently, on the xy plane, only the parts shown in Fig. 4.9 were used. One can see the difference by comparing Fig. 4.9 with the ideal track positions shown in Fig. 4.5.

Second, the first laser layers on each read-out side were excluded due to the effects of the gating grid and the trigger offset: Since the closest two micro-mirror bundles are located 10 cm (for the even laser rods) and 13 cm (for the odd laser rods) (see section 4.2.2) away from the gating grid, the first laser layer signals coming from the one 10 cm away from the gating grid may be distorted by the gating grid switching or may not be read out, i.e. cut by the readout of the FEE. This region is marked in Fig. 4.8 with a red circle.

Third, since the CE signal is received by all pads simultaneously, only part of the whole CE signal is sufficient for this study. Thus, in order to save memory and also reduce the processing time, after the first event was processed, only every 5th pad in a row was filled with the CE information.

Lastly, noise signals outside of a certain window around the three laser planes and the CE signal were cut. For this, the peaks were selected in the histogram shown in Fig. 4.8. For the CE peak a window of ± 10 time bins and for other peaks $4\times$'RMS' time bins around the 'mean' of each peak were chosen. In Fig. 4.8 the cut windows are depicted with red lines and the inset shows some noise signals which were cut.

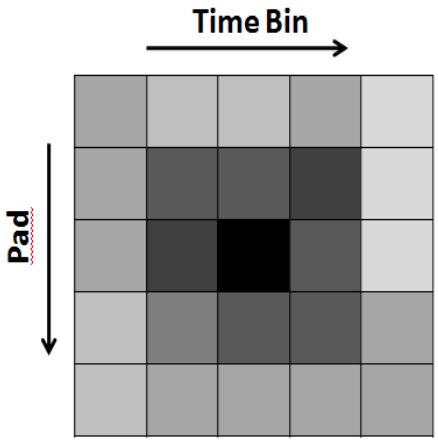

Figure 4.10: *Illustration of the* 5×5 *pad-time matrix. The amplitude of each cell is indicated by grey scale.*

4.3.2 Analysis

Having applied the cuts mentioned above, the data filling process of the histogram, for one burst, was completed. In the following, the processing of the data stored in this histogram is described.

4.3.2.1 Cluster Finding

Data processing starts with cluster finding. A cluster is a set of digits in pad and in time bin direction for one pad-row that is assumed to be generated by the same particle crossing the TPC volume. It is considered as the first step of the reconstruction process.

As mentioned in 'data filling' part, the histogram contains the ADC signals for each pad and time bin for all events within one burst. Namely, it has a pad-time matrix structure. In order to find the clusters, firstly, the peaks which will be used as seeds for clusters, were determined. For this, each pad-time cell having more than 5 ADC counts was compared to the surrounding cells to mark the peaks. The edge pads of the ROCs were excluded from the analysis.

Secondly, looping over all bins of the histogram within a certain time stamp window of ± 2 min (i.e. within a burst), all peaks were detected. Then, the center of gravity of the peak and surrounding pad-time cells within a 5×5 pad-time matrix was calculated according to the equations:

$$C_t = \frac{\sum_{t,b} m_{tb} r_t}{\sum_{t,b} m_{tb}}, \qquad C_p = \frac{\sum_{t,b} m_{tb} r_p}{\sum_{t,b} m_{tb}} \tag{4.4}$$

where r_t, r_p are the positions of the cells in time and pad direction, weighted by the bin content m_{tb} of the corresponding cell , and C_t, C_p are the center of gravity coordinates in time and pad directions, respectively. The peak was assigned to the center of the matrix, as shown in Fig. 4.10. This center of gravity is regarded as the local position of the cluster.

Each pad and its local coordinate are well defined in the Offline Calibration Data Base (OCDB), where the calibration and alignment data of the ALICE is stored, with respect to its specific integer pad number. Therefore, the center of the pad with the nearest integer

number to the C_p was taken to be the center of gravity instead of C_p, in order to obtain the local (x, y) (see section 2.3) position of the cluster.

Lastly, the z position of the cluster, which is the same for both local and global coordinate systems, was evaluated from the time bin and the default drift velocity information, which was also retrieved from the OCDB. As for the global x and y positions of the cluster, they were calculated by means of a coordinate transformation which is given by the equations (2.1) and (2.2).

4.3.2.2 Track Association

In order to get rid of the clusters that do not belong to laser tracks, the clusters, that are matching well with the ideal laser track positions in pad direction, were selected to be used for the rest of the analysis. The ideal laser track positions were extracted from the OCDB.

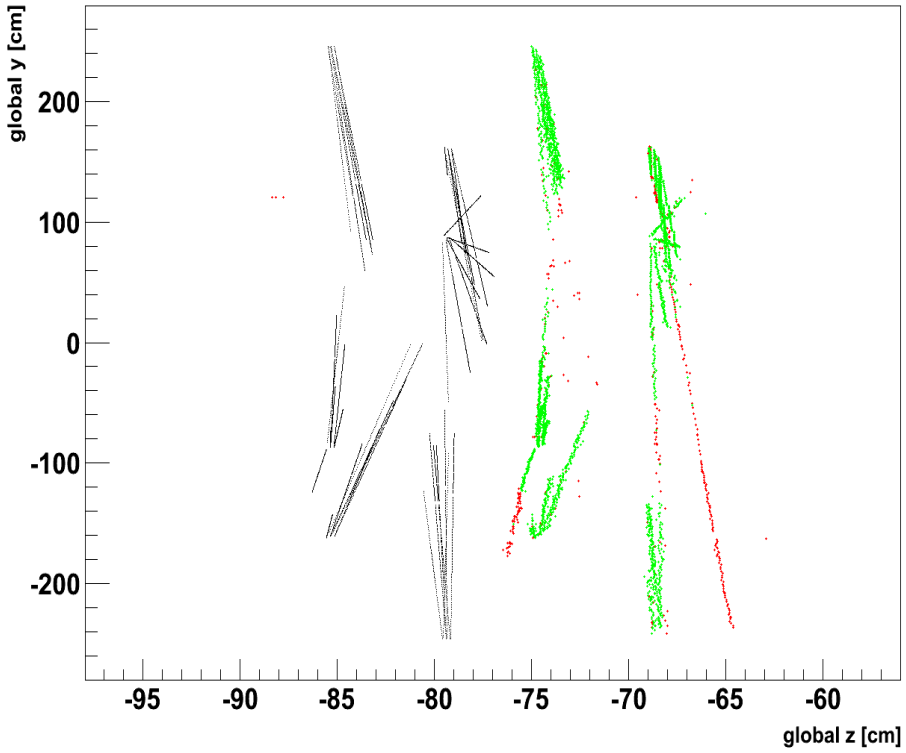

Figure 4.11: *The projection of the ideal, 'Associated' and 'Non-associated' clusters of one laser plane on the global yz plane, depicted in black, green and red colors, respectively.*

An ideal laser track is, actually, 159 consecutive clusters each corresponding to a separate row within one sector. Each ideal cluster contains its global (x, y, z) position, that is calculated from the measured positions of the micromirrors. Looping over all these ideal clusters, the ideal-reconstructed cluster pairs with the minimum distance in between were found. The minimum distance was searched for along the pad-row direction. In Fig. 4.11 the 'Non-associated', 'Associated' and ideal clusters for one laser plane are shown as a projection on the yz plane. The ~ 10 cm difference in between is mostly due to the trigger offset.

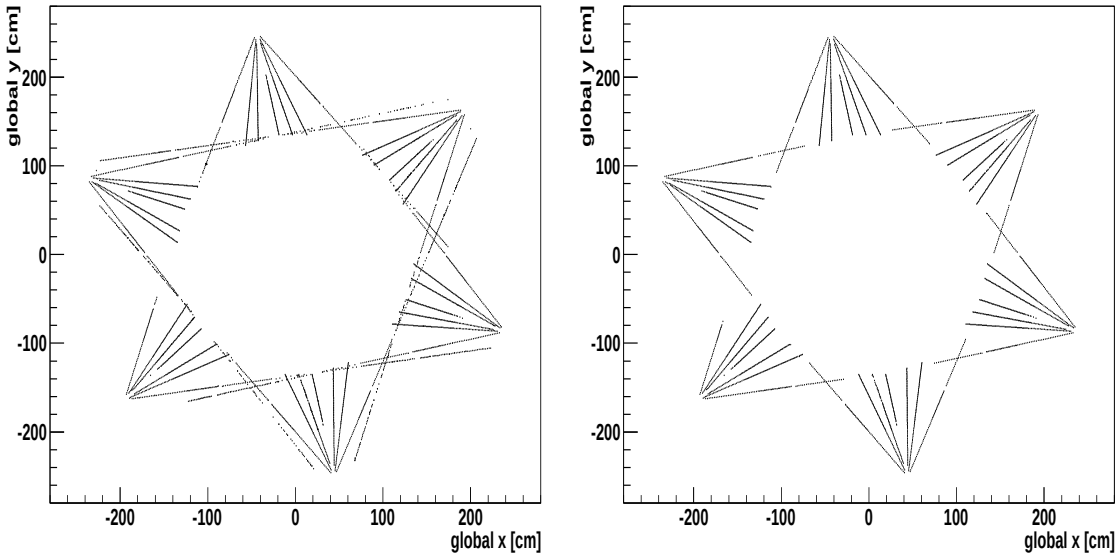

Figure 4.12: *The reconstructed clusters (left) and 'Associated Clusters' (right) as a projection on the global xy plane.*

In doing so, a more robust and practical use of clusters so called 'Associated Clusters' were obtained. Both, reconstructed and the associated clusters are shown in Fig. 4.12, as a projection on the xy plane. One can easily see on the left-hand plot that, only the laser tracks with the largest inclination angle can reach to the opposite side and contain much more clusters than the others. On the other hand, as seen on the right-hand plot, part of these tracks were cut due to the limited number of ideal clusters. The rest of the analysis was based on these 'Associated Clusters'.

During the development process, some more corrections were performed on the 'Associated Clusters':

First, since the reconstructed clusters on the tracks with the largest inclination angle may have been wrongly associated to the ideal clusters owing to the contribution of the laser tracks coming from the micromirror bundle on the opposite side, they were not included in the analysis. Fig. 4.13 shows the projection of a part of one laser plane on the global xy plane. As seen, the laser tracks emerging from bottom right and top left corner reach to the opposite side and at some point they cross each other. Since the associated clusters were based on the minimum distance calculation between reconstructed and ideal clusters, the crossing regions and also the very far end of these tracks may cause some mismatches.

Second, a cut was also put on the cluster number within one laser track. The laser tracks having less than 30 clusters were not included in the analysis. This cut was introduced to avoid effects from statistical fluctuations resulting from the low intensity laser tracks. In Fig. 4.14 some low intensity tracks are displayed. It is easily seen that, the laser tracks with few cluster points are not aligned linearly, as they are supposed to be. The reason for this could be the wrong association to clusters. In the regions with few clusters, some of the noise clusters might be mixed up with the laser track clusters.

Third, due to the finite speed of light and the layout of the laser distribution system, the light arrives at different positions at different times. This causes the simultaneity of

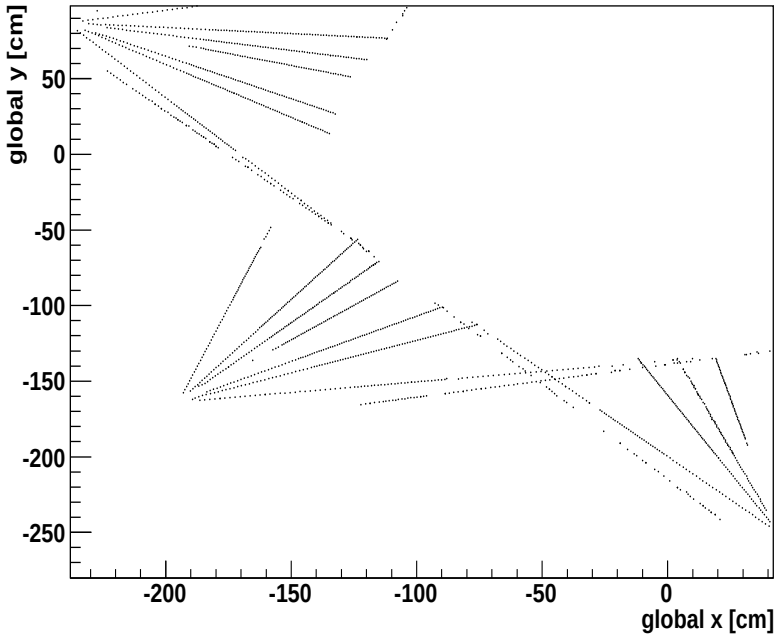

Figure 4.13: *Projection of a part of a laser plane on the global xy plane.*

the laser tracks to be broken. The relative error of the measurement is given by:

$$\Delta L \cdot \frac{\nu_d}{c} \approx \Delta L \cdot 8.8 \times 10^{-5} \tag{4.5}$$

where c is the speed of light, ν_d ($\sim 2.64 cm/\mu s$) is the drift velocity and ΔL is the distance between any two ionisation points. One can easily find the error of about 1.5 mm, for the maximum ΔL, which is about 12 m. The correction for this effect was also implemented, even though it provides only a slight improvement.

Lastly, a systematic offset, which causes a small tail in the residuals shown in Fig. 4.15, between the ideal laser track positions and the CE position was found. This was corrected by setting the relative alignment of the CE position to -0.355 cm for A- and 0.15 cm for C-Side. As seen on the left column in Fig. 4.15, this offset was removed after the alignment.

4.3.2.3 Fitting

After these corrections, a fit was performed on the ideal clusters as function of the associated clusters, so that the drift velocity correction factors were extracted as the fit parameters. A similar fit procedure to the offline laser calibration was used: separate fits for A- and C-Side and a common fit for the whole TPC.

In the fitting procedure, a linear fitter was used. The reasons for the choice of the linear fitter were: It is considerably faster than general non-linear fitters, doesn't require to set the initial values of parameters and for very large sets of points the χ^2 is calculated more precisely. The standard errors on parameters, however, are not calculated.

Since the associated cluster positions were defined with 3 linearly independent variables: drift length, global y gradient and radial position, as well as the trigger offset, the following corrections are required:

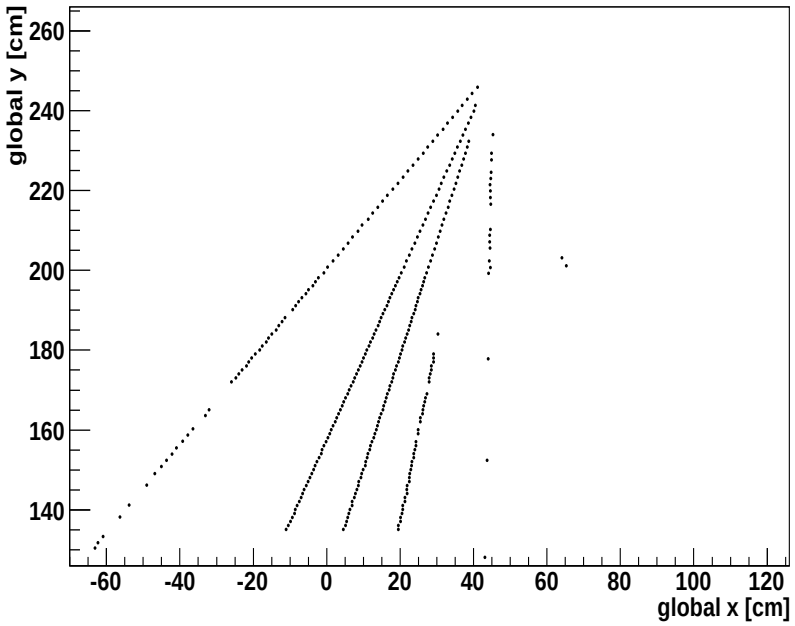

Figure 4.14: *Seven laser tracks emerging from one micro-mirror bundle with two of them are completely lost and two have low intensity.*

- Trigger offset,
- Mean drift velocity correction,
- Relative global y gradient resulting from temperature and pressure gradients,
- Radial deformation resulting from the CE geometry.

Therefore, the following formula was chosen as the fit function:

$$f = \alpha_0 + \alpha_1 l_d + \alpha_2 \frac{y_i}{250} \frac{l_d}{L_d} + \alpha_3 \left(250 - R_m\right) \tag{4.6}$$

where α_i are the correction factors corresponding to the terms given above, l_d is the drift length of the ideal cluster point, L_d is the whole drift length (-250 cm for C- and 250 cm for A-Side), y_i is the global y coordinate of the ideal cluster point and R_m is defined as:

$$R_m = \sqrt{x_m^2 + y_m^2} \tag{4.7}$$

where x_m, y_m are the global x, y coordinates of the reconstructed clusters.

The obtained mean drift velocity correction factor (α_1) distribution over all runs are shown in Fig. 4.16. One can easily infer from the figure that the maximum change in the drift velocity is on the level of several percent. The reason for this is that, these results were not yet corrected with the temperature and pressure, that have a big impact on the drift velocity (see section 4.1.1).

Furthermore, in order to clear away the outlier clusters and to obtain a better fit result, the fit was performed in three iterations. First, the data was fitted without any cut applied

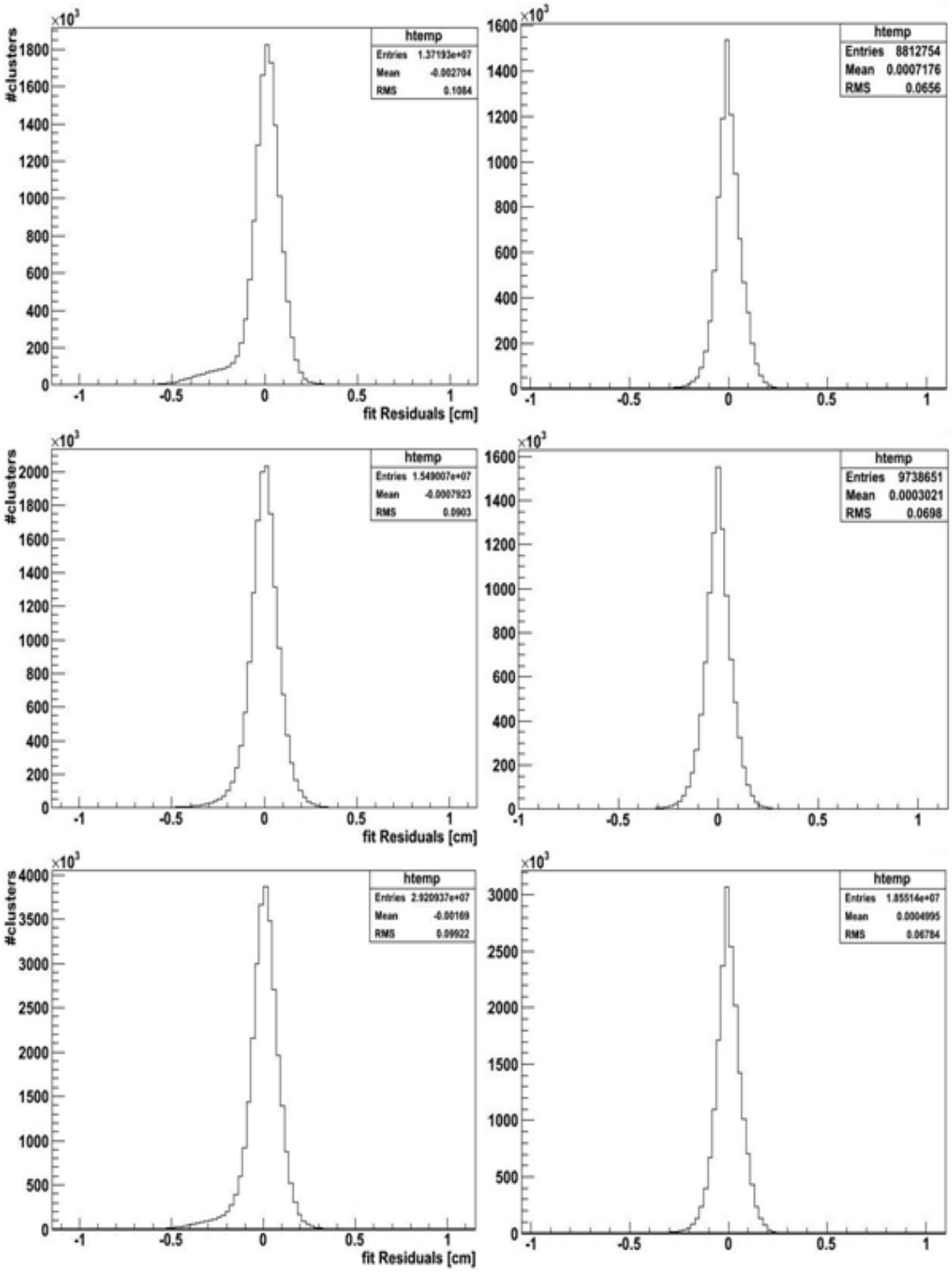

Figure 4.15: *The residuals before (left column) and after (right column) the corrections were applied to the 'Associated Clusters' for three cases of the linear fit; (from top to bottom) A-Side, C-Side and the whole TPC.*

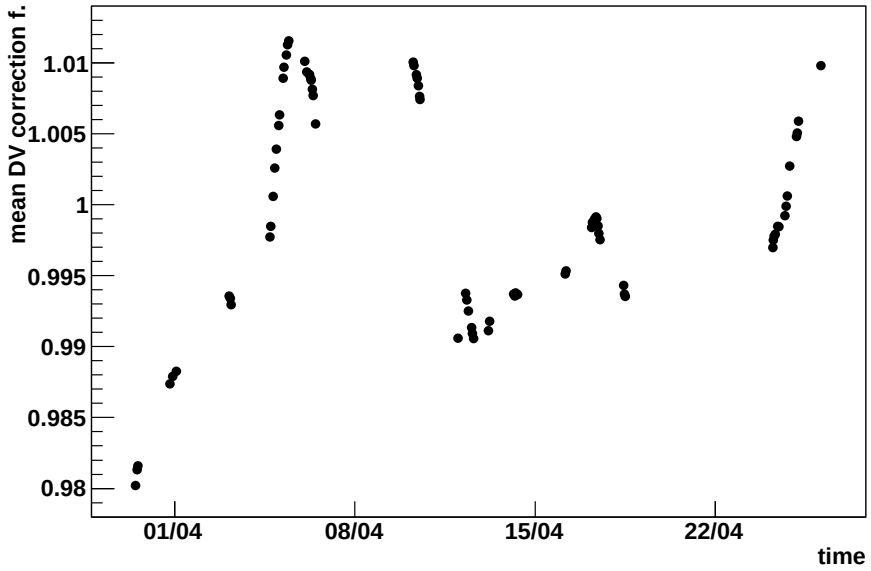

Figure 4.16: *Mean drift velocity correction factor (α_1) distribution over all runs.*

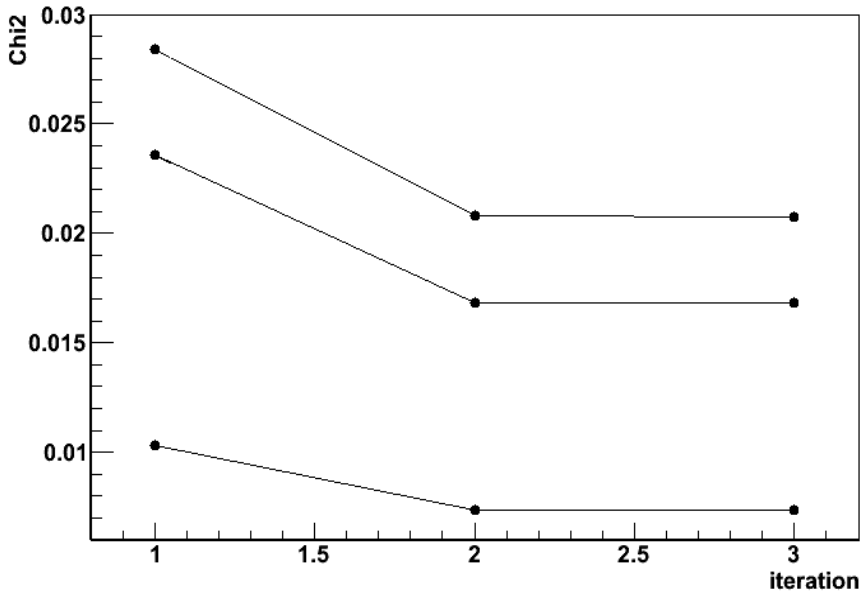

Figure 4.17: *The effect of the three iterations on the χ^2 values, while fitting the clusters. The lines connect the χ^2 points of one burst. From bottom to top; first, second and third burst.*

and then, consecutively within a window of 1 cm and 0.8 cm residuals. The effect of this iteration can be seen on the χ^2 values in Fig. 4.17. The figure shows the χ^2 results of a run with 3 bursts. While performing the fit, the uncertainty of the reconstructed cluster points were set to 1. Therefore, the decreasing χ^2 can be interpreted as the increasing 'resolution' of the points.

In the end, all the correction factors (α_i) were stored in three separate arrays: for A-Side,

C-Side and the whole TPC. The χ^2 and 'number of points' information were also filled into these arrays to be used for testing of the performance of the method, as well as the data quality.

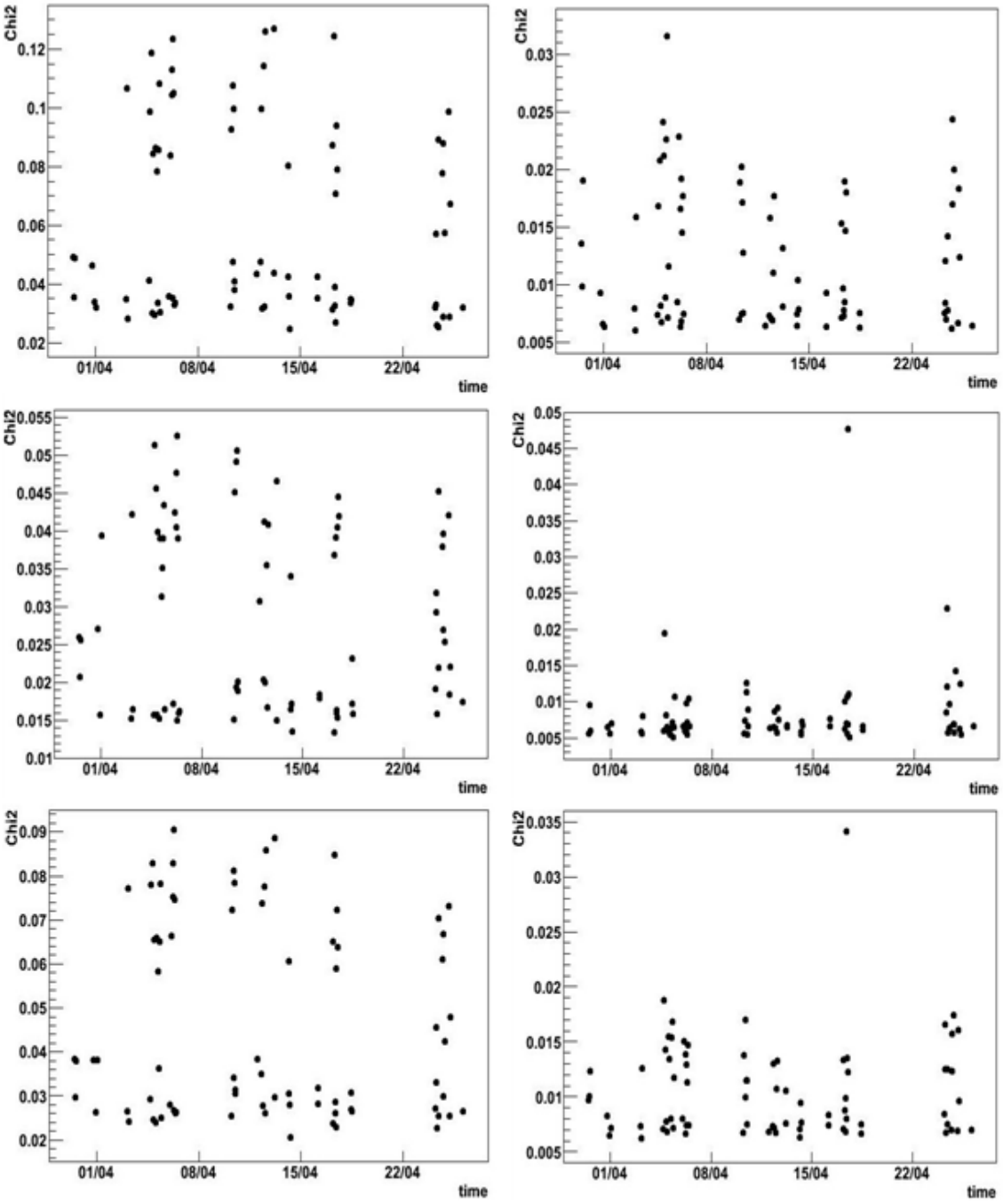

Figure 4.18: *The χ^2 distributions before (left column) and after (right column) the corrections were applied to the 'Associated Clusters' for three cases of the linear fit; (from top to bottom) A-Side, C-Side and the whole TPC.*

4.3.3 Results

In this study, 45 physics runs, taken in April 2010, were used. The selection of the laser events was done by means of the laser trigger class. During the analysis raw data in root format were used as an input. The Laser event selection and data taking processes are described in Appendix A.

To test the performance of the method, the χ^2 distribution and residuals were used as benchmarks. Fig. 4.18 illustrates the change in the χ^2 distributions and Fig. 4.15 in the residuals before and after the corrections (see section 4.3.2.2) were applied to the 'Associated Clusters'.

After achieving reasonable residual with an average 'RMS' of about ~ 0.6 mm (Fig. 4.15), which is comparable to the measured space point resolution of ~ 0.5 mm [15], the outcome of the online method was compared with the offline methods: the offline laser calibration method and the TPC-ITS track matching method.

The online laser calibration method provides the correction factor x $(= \alpha_1)$ derived in section (4.1.2.2). However, the comparison was carried out with respect to the $k_0(t)$ factor in equation (4.3) which covers the influence of the gas composition and electric field changes. To obtain the $k_0(t)$ factor, the pressure and temperature corrections, i.e. T/P correction was subtracted from x. The T/P correction was calculated in the same way as it is done in the offline code:

$$\alpha_{T/P} = k_{T/P} \frac{T_m/P_m - T_n/P_n}{T_n/P_n} \tag{4.8}$$

where T_m and P_m are the measured and T_n and P_n are the nominal temperature and pressure values, respectively. Further, the $k_{T/P}$ factor was retrieved from the OCDB as 1 for the analysed data taking period.

After having achieved the $k_0(t)$ component of the drift velocity correction factor x, the OCDB entries of the online results were created and both online and offline results were displayed and compared in a graphical interface which enabled us to perform a crosscheck between them. Hereafter, the $k_0(t)$ factor is called 'drift velocity correction factor'.

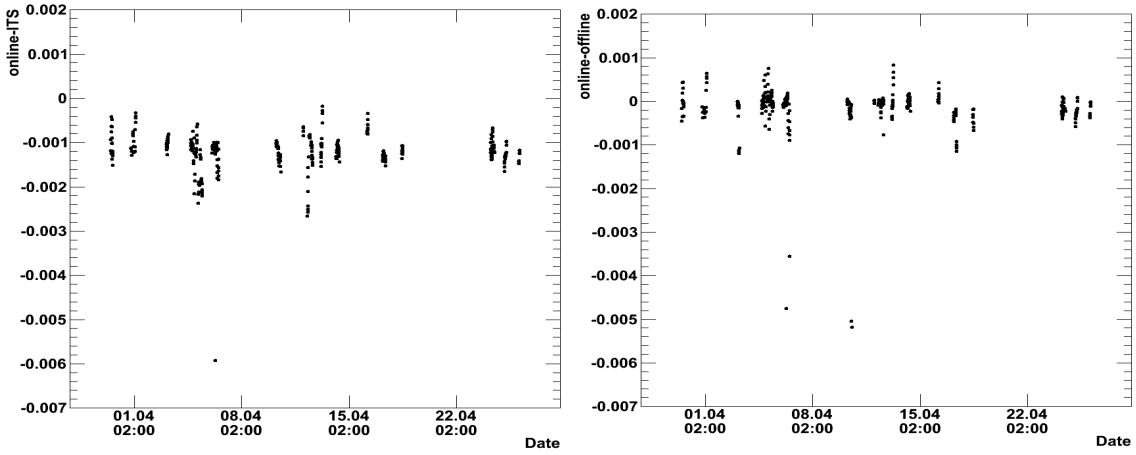

Figure 4.19: *The distribution of the drift velocity correction factor difference between online and offline laser calibration methods (left) and between online laser calibration and TPC-ITS track matching methods (right) with a cut of 1 hour distance in time to the last calibration time stamp.*

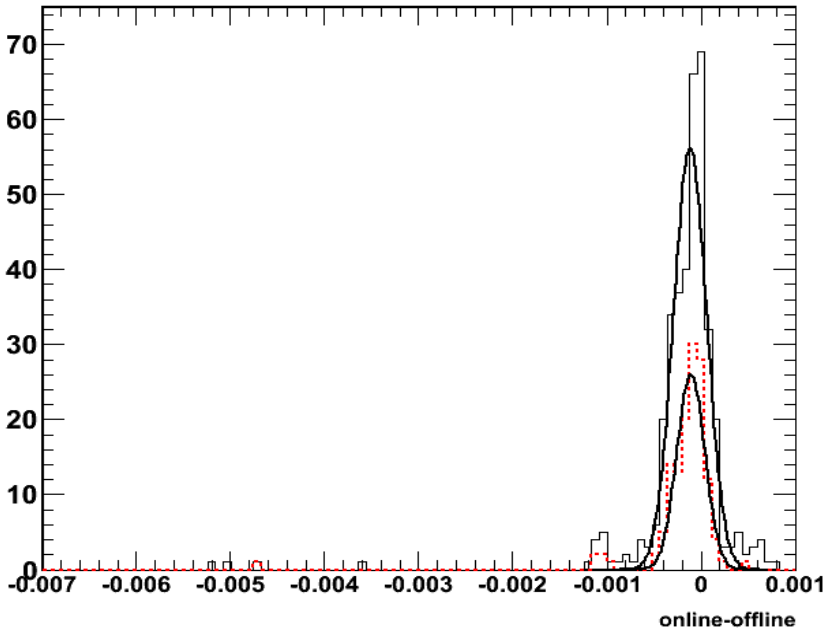

Figure 4.20: *The histogram of the drift velocity correction factor difference between online and offline laser calibration methods with the cuts of 1 hour (black straight lines) and 17 min (red dashed lines) distance in time to the last calibration time stamp.*

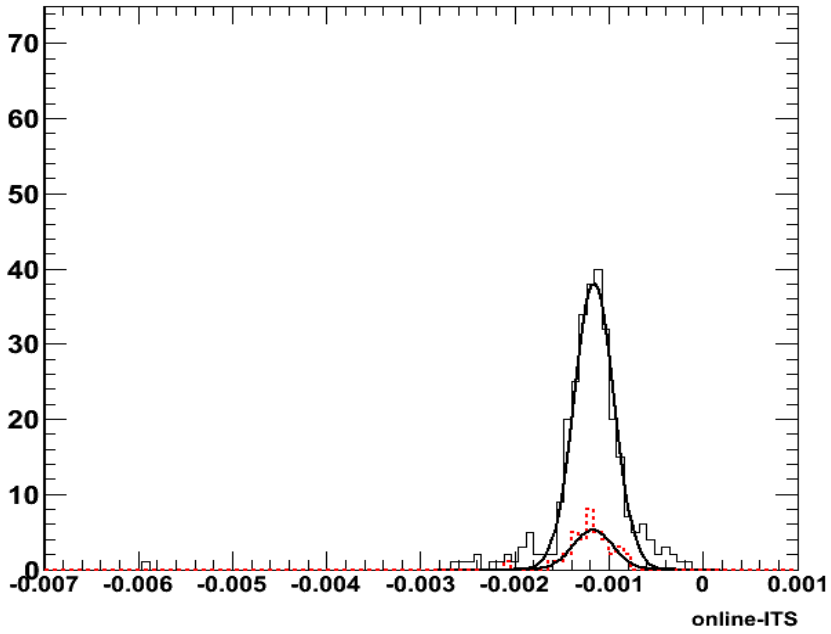

Figure 4.21: *The histogram of the drift velocity correction factor difference between online laser calibration and TPC-ITS track matching methods with the cuts of 1 hour (black straight lines) and 17 min (red dashed lines) distance in time to the last calibration time stamp.*

Fig. 4.19 shows the distribution of the drift velocity correction factor difference between

online and offline methods with a cut of 1 hour distance in time to the last calibration time stamp. The ~ -0.001 shift results from the fact that the TPC was not fully calibrated during the time included in the analysis [47].

Fig. 4.20 and Fig. 4.21 show the distribution of the deviation of online laser calibration method around the offline laser calibration and TPC-ITS track matching methods, respectively. In these figures two different cuts are displayed: 1 h and 17 min distance in time to the last calibration time stamp. One can see that, a big part of the outliers were removed by decreasing the cut from 1 h to 17 min. Nevertheless, the reasons of the outliers and the asymmetry of the peak are still under investigation.

In order to make a practical crosscheck between Fig. 4.20 and Fig. 4.21, Gauss fits, which are excluding the outliers, were performed on all histograms in these figures. The sigma and mean of the Gauss fits are summarized in Table 4.1.

	online-offline		**online-ITS**	
Cut	**Sigma** $[\times 10^{-4}]$	**Mean** $[\times 10^{-4}]$	**Sigma** $[\times 10^{-4}]$	**Mean** $[\times 10^{-4}]$
1 h	1.76594	-1.17060	2.10121	-11.6146
17 min	1.48846	-1.08205	2.11641	-11.7400

Table 4.1: *The mean and sigma values of the Gauss fits of the corresponding histograms for the cuts of 1 h and 17 min distance in time to the last calibration time stamp.*

One can easily infer from the Table 4.1 that, the agreement between the online and offline laser calibration methods is slightly better than the agreement between the online laser calibration and the TPC-ITS track matching methods. This makes sense because both online and offline laser calibration methods calculate the drift velocity correction factor making use of the information from TPC only while the TPC-ITS track matching method additionally uses the ITS track information which is completely independent of the TPC. That is why, the online and offline laser calibration methods are expected to be more consistent.

The drift velocity correction factor distribution over all runs for all methods with 17 min cut is displayed in Fig. 4.22. Since, the results shown here are T/P corrected, the maximum change in the drift velocity is on the level of several permille, which is mostly due to the gas composition and electric field changes in time.

Eventually, having achieved a reasonable agreement between the online laser calibration method and the offline methods on the level of about 2×10^{-4}, the study was finalized and the whole functionality of the code was implemented into a calibration class. The online drift velocity calibration method is currently being used in the first reconstruction pass in ALICE. Nevertheless, it is still open to further developments, as are all calibration studies.

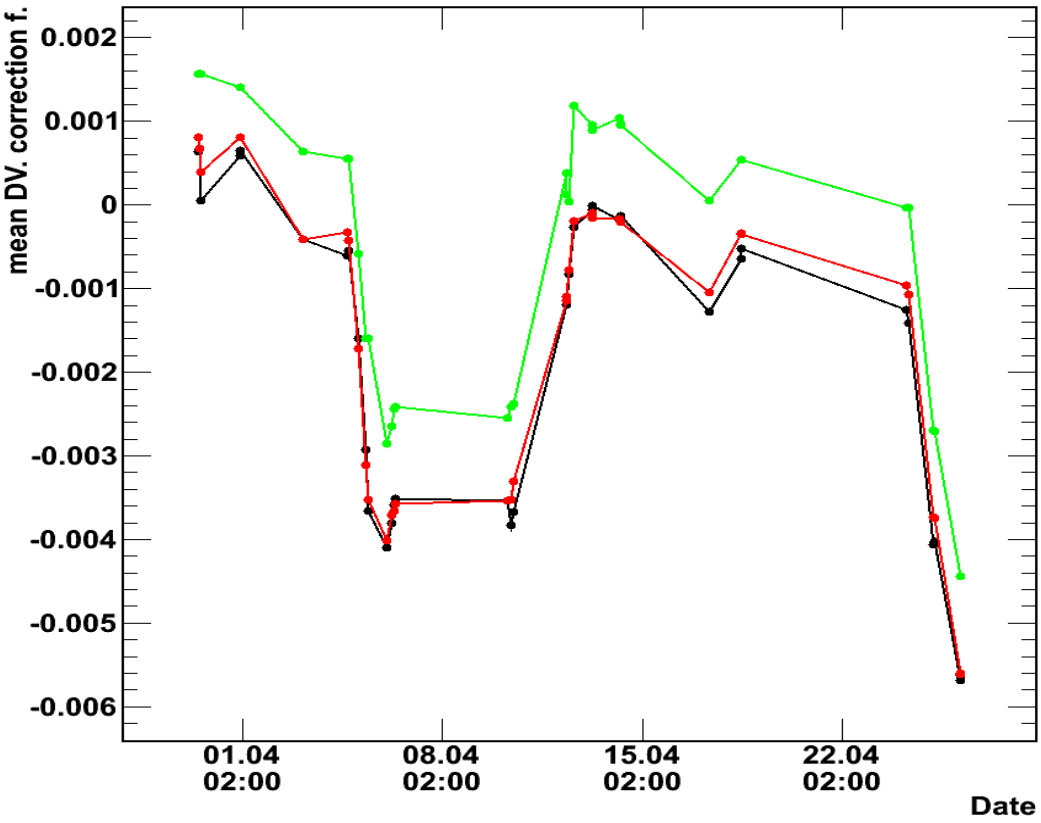

Figure 4.22: *Drift velocity correction factor distribution over all runs for online (black) and offline (red) laser calibration methods and TPC-ITS (green) track matching method with a cut of 17 min distance in time to the last calibration time stamp.*

Summary and Outlook

This thesis presents an online method for the calibration of the drift velocity making use of the ALICE TPC laser system. It is aimed to acquire a fast and reliable calibration tool which provides drift velocity calibration parameters to be used in the offline reconstruction.

The analysis was carried out on 45 physics runs, taken in April 2010. As an input, raw data, which was retrieved from the laser events interspersed between physics triggers, was used. The data was stored in multi-dimensional histograms for each set of events, so called 'burst'. Overall analysis was performed on these histograms iteratively. At the stage of data filling, some cuts were applied on the data not only to reduce the data size but also to exclude most of the noise signals and a part of the data which is affected by distortions.

Looping over all pad-time cells, the clusters were calculated as the center of gravity of pad-time cells within a 5×5 pad-time matrix. These reconstructed clusters were then associated to the ideal clusters by selecting the ones having minimum distance to the ideal cluster points, that are available in the Offline Calibration Database (OCDB).

After having applied some more corrections on the associated clusters, a linear fit was performed on the ideal clusters as a function of the associated clusters. The drift velocity correction factors, as well as the χ^2 values, were obtained as fit parameters. To test the performance of the method, the χ^2 distribution and residuals were used as the two benchmarks.

The results of the online method were compared to the other offline methods: the offline laser calibration method and the TPC-ITS track matching method. Even though no tracking information was used, the agreement achieved with the offline methods including tracking is on the level of 2×10^{-4}. Considering the required drift velocity resolution of the order 10^{-4}, this is a rather satisfactory result. Nevertheless, the method is still open to further improvements.

In the end, the whole functionality of the code was implemented into a calibration class. The method is currently being used in the offline reconstruction chain of ALICE.

Appendices

A Access to the Raw Data

A.1 How to Select the Laser Events?

This is the first step in which we select the laser events, that will be used in the analysis, by means of the laser trigger class;

```
AliCDBManager *man=AliCDBManager::Instance();
man->SetDefaultStorage("local:///lustre/alice/alien/alice/data/2010/OCDB");
man->SetRun(run);
AliCDBEntry *entry=man->Get(AliCDBPath("GRP/CTP/Config"));
AliTriggerConfiguration* trg=(AliTriggerConfiguration*)entry->GetObject();
TIter next(&trg->GetClasses());
TObject *o=0x0;
ULong64_t classMask=100000000;
while ( (o=next()) ){
   TString className(o->GetName());
   if (className.Contains("C0LSR-ABCE"))
      AliTriggerClass *cl=(AliTriggerClass*)o;
      classMask=cl->GetMask();
      printf("Found laser class Mask: %u  n",(UInt_t)classMask);
      break;
   }
}
if (classMask==100000000) {
   printf("No Laser trigger class mask found! No processing.");
   return;
}
```

A.2 How to Access the Digits?

After selecting the necessary events, we now access the digits in the raw data via a raw reader:

```
AliTPCCalibCE *ce=new AliTPCCalibCE;
AliRawReaderRoot *rawReader=new AliRawReaderRoot(filename);
while (reader->NextEvent()){
   if ( rawReader->GetClassMask()!=classMask ) return;
   ce->ProcessEvent(rawReader);
}
ce->Analyse();
TFile f("CalibCE.root","recreate");
```

```
ce->Write("tpcCalibCE");
f.Close();
delete rawReader;
delete ce;
```

The next step is to fill the multi-dimensional histogram, so called “ThnSparse” and to analyse the data.

B Some of the Functions Used in the Analysis

The whole functionality of the code was implemented into a calibration class so-called "AliTPCCalibCE". In the following, the functions related to the online method are summarized: **ProcessBunch():**

- Fill the histogram,
- Exclude IROCs,
- Accept the bunches with a reasonable range,
- Exclude first laser layer,
- After the first event only fill every 5th bin in a row with the CE information.

FindLaserLayers(): Find the laser layer and CE positions.

CreateDVhist(): Setup the histogram for the drift velocity determination.

FindLocalMaxima():

- Loop over all entries in the histogram,
- Find central electrode position separately for IROC, OROC, A-, C-Side,
- Apply ADC, timestamp and 'edge pad' cuts,
- Find the local maxima, namely the center of gravity points (COG),
- Perform the coordinate transformations on the COG points,
- Correct for the travel time effect of light,
- Create the "*clusters*" TTree for monitoring purposes,

AnalyseTrack():

- Calculate the minimum distances between ideal and reconstructed clusters,
- Analyse the tracks,
- Create the "*tracks*" Tree for monitoring purposes.

FindLaserTrackID(): Find the clusters, which are closest to the ideal clusters.

CalculateDV():

- Calculate the drift velocity from the reconstructed clusters associated to the ideal laser tracks,
- Perform the linear fitter in three iterations and extract the drift velocity correction factors.
- Exclude the tracks which have the biggest inclination angle,
- Exclude the low intensity tracks,
- Create the "*DriftV*" TTree for monitoring purposes.

Bibliography

[1] D. H. Perkins, *Introduction to High Energy Physics* (Cambridge University Press, 2000).

[2] L. P. Csernai, *Introduction to Relativistic Heavy Ion Collisions* (John Wiley and Sons Ltd, 1994).

[3] P. Aurenche, *The standard model of particle physics*, 1997, arXiv:hep-ph/9712342.

[4] M. Gell-Mann, *A Schematic Model of Baryons and Mesons*, Phys. Lett. **8**, 214 (1964), doi:10.1016/S0031-9163(64)92001-3.

[5] D. Griffiths, *Introduction to Elementary Particles* (John Wiley and Sons, Inc., 1987).

[6] D. J. Gross, *Twenty five years of asymptotic freedom*, Nucl. Phys. Proc. Suppl. **74**, 426 (1999), arXiv:hep-th/9809060, doi:10.1016/S0920-5632(99)00208-X.

[7] U. W. Heinz, *The little bang: Searching for quark-gluon matter in relativistic heavy-ion collisions*, Nucl. Phys. **A685**, 414 (2001), arXiv:hep-ph/0009170, doi:10.1016/S0375-9474(01)00558-9.

[8] U. W. Heinz, *Concepts of heavy-ion physics*, 2004, arXiv:hep-ph/0407360.

[9] D. Antonczyk, *Detailed Analysis of Two Particle Correlations in Central Pb-Au Collisions at 158 GeV per Nucleon*, PhD thesis, Technische Universität, Darmstadt, 2006.

[10] P. Giubellino, *The ALICE detector at LHC*, Nucl. Instr. Meth. A **344**, 27 (1994).

[11] ALICE Collaboration, *ALICE: Physics Performance Report, Volume I*, J. Phys. **G30**, 1517 (2004), doi:10.1088/0954-3899/30/11/001.

[12] P. Kuijer, *The Alice experiment at the CERN LHC*, Nuclear Physics B **117**, 62 (2003).

[13] E. Vercellin, *The ALICE experiment at the LHC*, Nuclear Physics A **805**, 511 (2008).

[14] ALICE Collaboration, *The ALICE experiment at the CERN LHC*, JINST **3**, S08002 (2008), doi:10.1088/1748-0221/3/08/S08002.

[15] ALICE TPC Collaboration, *The ALICE TPC, a large 3-dimensional tracking device with fast readout for ultra-high multiplicity events*, Nucl. Instr. Meth. A **622**, 316 (2010).

[16] ALICE Collaboration, *Technical Design Report of the Inner Tracking System*, CERN/LHCC 99-12, 1999.

[17] ALICE Collaboration, *Technical Design Report of the Time Projection Chamber*, CERN/LHCC 2000-001, 2000.

[18] ALICE Collaboration, *Technical Design Report of the Transition Radiation Detector*, CERN/LHCC 2001-021, 2001.

[19] ALICE Collaboration, *Technical Design Report of the Time of Flight System*, CERN/LHCC 2000-012, 2000.

[20] ALICE Collaboration, *Technical Design Report of the High Momentum Paricle Identificatino Detector*, CERN/LHCC 98-19, 1998.

[21] ALICE Collaboration, *Technical Design Report of the Photon Spectrometer*, CERN/LHCC 99-4, 1999.

[22] ALICE Collaboration, *The Electromagnetic Calorimeter Addendum to the Technical Proposal*, CERN-LHCC-2006-014, 2006.

[23] ALICE Collaboration, *Technical Design Report of the Dimuon Forward Spectrometer*, CERN/LHCC 99-22, 1999.

[24] ALICE Collaboration, *Technical Design Report of the Zero Degree Calorimeter (ZDC)*, CERN/LHCC 99-5, 1999.

[25] ALICE Collaboration, *Technical Design Report of the Photon Multiplicity Detector (PMD)*, CERN/LHCC 99-32, 1999.

[26] ALICE Collaboration, *Technical Design Report on Forward Detectors: FMD, T0, V0*, CERN-LHCC-2004-025, 2004.

[27] L. Betev and P. Chochula, *Definition of the ALICE Coordinate System and Basic Rules for Sub-detector Components Numbering*, ALICE-INT-2003-038 (2003).

[28] J. Wiechula, *Commissioning and Calibration of the ALICE-TPC*, PhD thesis, Johann Wolfgang Goethe-Universität, Frankfurt am Main, 2008.

[29] C. Lippmann and D. Vranić, *Alice TPC Numbering Conventions*, http://lippmann.web.cern.ch/lippmann/TPC/num.pdf.

[30] V. Lindenstruth *et al.*, *Real-time TPC analysis with the ALICE High-Level Trigger*, Nucl. Instr. Meth. A **534**, 47 (2004), doi:10.1016/j.nima.2004.07.057.

[31] ALICE Collaboration, *ALICE Technical Design Report of the Computing*, CERN-LHCC-2005, 2005.

[32] *ALICE Offline Bible*, http://aliweb.cern.ch/Offline/AliRoot/Manual.html.

[33] L. Musa, *The Time Projection Chamber for the ALICE experiment*, Nuclear Physics A **715**, 843c (2003).

[34] C. Garabatos, *The ALICE TPC*, Nucl. Instr. Meth. A **535**, 197 (2004), doi:10.1016/j.nima.2004.07.127.

[35] L. Musa *et al.*, *The ALICE TPC front end electronics*, in *IEEE Nuclear Science Symposium* Vol. 5, pp. 3647–3651, 2003, doi:10.1109/NSSMIC.2003.1352697.

[36] R. Veenhof, *Choosing a gas mixture for the ALICE TPC*, ALICE-INT-2003-29 (2003).

[37] P. S. Frankenfeld, U. and H. Schmidt, *Temperature Monitoring System for the ALICE TPC*, ALICE-EN-2005-001 (2005).

[38] J. Wiechula, *Commissioning and Calibration of the ALICE TPC*, Nuclear Physics A **830**, 531 (2009).

[39] U. Frankenfeld, *Commissioning of the ALICE Time Projection Chamber*, Nucl. Instr. Meth. A **581**, 179 (2007), doi:10.1016/j.nima.2004.07.072.

[40] W. Blum and L. Rolandi, *Particle Detection with Drift Chambers* (Springer-Verlag, 1994).

[41] D. Vranic, private communication.

[42] H. J. Hilke, *Detector calibration with lasers – A review*, Nucl. Instr. Meth. A **252**, 169 (1986), doi:10.1016/0168-9002(86)91177-0.

[43] J. Wiechula *et al.*, *High-precision measurement of the electron drift velocity in Ne-CO2*, Nucl. Instr. Meth. **A548**, 582 (2005), doi:10.1016/j.nima.2005.05.031.

[44] G. Renault, B. S. Nielsen, J. Westergaard and J. J. GaardhOJe, *The laser of the ALICE time projection chamber*, 2007, arXiv:nucl-ex/0703042.

[45] B. Nielsen, J. Westergaard, J. Gaardhoje and A. Lebedev, *Design Note on the ALICE TPC laser calibration system*, ALICE-INT-2002-022, 2002.

[46] A. Lebedev, *A laser calibration system for the STAR TPC*, Nucl. Instr. Meth. A **478**, 163 (2002).

[47] M. Ivanov, private communication.

List of Figures

List of Tables

Acknowledgements

This work would have not been possible without the support of many people to whom I would like to express my gratitude. First of all, I would like to thank Prof. Dr. Harald Appelshäuser and Prof. Dr. Hans Rudolf Schmidt for their support and giving me the opportunity to write this thesis and participate in this fascinating experiment. Likewise, many thanks to Prof. Dr. Peter Braun Munzinger who gave me the opportunity to work in the ALICE group at GSI. Of course, many thanks also to the ALICE GSI team for the assimilation. It is a wonderful experience to work with them.

In particular, I am heartily thankful to my supervising tutor Dr. Jens Wiechula, whose supervision and support from the preliminary to the concluding level enabled me to develop an understanding of the subject. I have learnt a lot from him. Without his guidance I could not have even imagined to get to this point. I also would like to thank Dr. Marian Ivanov. His recommendations and suggestions have been invaluable for the project and for software improvement.

Many thanks to the members of the ALICE group in Frankfurt, IKF (Institut für Kernphysik) for their cooperation, as well as FIAS (Frankfurt Institute for Advanced Studies) for the financial support. I especially owe my deepest gratitude to Prof. Dr. Henner Büsching, Dr. Rainer Renfordt and Jutta Berschin for their constant help in so many aspects.

Special thanks should be given to my student colleagues Markus Koehler, Philipp Luettig, Moritz Pohl, Patrick Reichelt, Amely Tampe, and Anna Bernhard for their community and help in many ways throughout my studies.

Special thanks to my family, especially my sister Dilek Yıldırım and her husband Osman Yıldırım, for the moral support they have given me throughout my education.

Lastly, words alone cannot express the thanks I owe to Prof. Dr. Metin Subaşı and Sedat Altınpınar, for their encouragement, guidance and support.